1-2023

Simplified Mass and Inertial Estimates for Aircraft with Components of Constant Density

Benjamin C. Moulton
Utah State University, ben.moulton@usu.edu

Douglas F. Hunsaker
Utah State University, doug.hunsaker@usu.edu

Recommended Citation

Moulton, B. C., and Hunsaker, D. F., "Simplified Mass and Inertial Estimates for Aircraft with Components of Constant Density," AIAA SCITECH 2023 Forum, January 2023, AIAA-2023-2432 DOI: 10.2514/6.2023-2432

Simplified Mass and Inertial Estimates for Aircraft with Components of Constant Density

Benjamin C. Moulton* and Douglas F. Hunsaker†
Utah State University, Logan, Utah 84322-4130

Aircraft mass and inertial properties are required for predicting the dynamics and handling qualities of aircraft. However, such properties can be difficult to estimate since these depend on the external shape and internal structure, systems, and mass distributions within the airframe. Mass and inertial properties of aircraft are often predicted using computer-aided design software, or measured using various experimental techniques. The present paper presents a method for quickly predicting the mass and inertial properties of complete aircraft consisting of components of constant density. Although the assumption of constant density may appear limiting, the method presented in this paper can be used to approximate mass properties of complex internal structures. Inertial estimates for rectangular cuboids, cylinders, spheres, wing segments, and rotors are presented here. The influence of geometric properties of wing segments such as sweep, taper, airfoil geometry, and dihedral are included. The utility of the method is presented and the accuracy is evaluated with various test cases.

I. Nomenclature

a	=	thickness distribution coefficients
b	=	semispan length
c_r	=	root chord length
c_t	=	tip chord length
d	=	diameter
$[\mathbf{E}]$	=	identity matrix
e_0, e_x, e_y, e_z	=	quaternion orientation components
g	=	acceleration due to gravity
$[\mathbf{h}]$	=	angular momentum vector
h_x, h_y, h_z	=	angular momentum about the x, y, and z-axes
h	=	height
$[\mathbf{I}]$	=	inertia tensor
I_{xx}	=	moment of inertia about the x axis
I_{xy}	=	product of inertia calculated from x and y coordinates
I_{xz}	=	product of inertia calculated from x and z coordinates
I_{yy}	=	moment of inertia about the y axis
I_{yz}	=	product of inertia calculated from y and z coordinates
I_{zz}	=	moment of inertia about the z axis
l	=	length
m	=	mass
M_{xy}	=	moment in the z-direction
M_{xz}	=	moment in the y-direction
M_{yz}	=	moment in the x-direction
N_b	=	number of blades on a rotor
$[\mathbf{R}]$	=	rotation matrix
R	=	radius in cylinder and sphere coordinate system
$\mathbf{r}$	=	length vector to cg location

*PhD Student, Mechanical and Aerospace Engineering, 4130 Old Main Hill, AIAA Student Member
†Associate Professor, Mechanical and Aerospace Engineering, 4130 Old Main Hill, AIAA Senior Member

r	=	radius in rotor coordinate system
S	=	wing integration coefficient
$\mathbf{s}$	=	length vector
T	=	rotor integration coefficient
t	=	maximum airfoil thickness
V	=	volume
W	=	Weight
x, y, z	=	coordinates in the aircraft coordinate frame
$\hat{x}, \hat{y}, \hat{z}$	=	change of variables coordinates in the wing coordinate frame
$\bar{x}, \bar{y}, \bar{z}$	=	coordinates of the center of gravity
x_a, y_a	=	coordinates in the airfoil coordinate frame
x_m	=	location of maximum thickness in airfoil coordinates for a diamond-shaped airfoil
Γ	=	dihedral angle
γ	=	rotor planform coefficient
δ	=	left wing / right wing sign coefficient
κ	=	wing planform coefficient
Λ	=	quarter-chord sweep angle
μ	=	airfoil thickness distribution
ρ	=	density
τ	=	percent maximum airfoil thickness
υ	=	thickness distribution coefficient
ϕ	=	bank angle
φ	=	angular coordinate in cylindrical and rotor coordinate frames
ψ	=	azimuth angle
ω	=	angular rate vector
ω_x	=	angular rate about the rotor x-axis

II. Introduction

Determining the moments and products of inertia of an aircraft is a crucial step in designing an aircraft. This is partially due to the fact that the moments and products of inertia are required to determine the dynamic modes of an aircraft. The dynamic analysis of an aircraft directly affects control surface sizing in preliminary design phases [1]. Inertial metrics can also be used to determine the aircraft stability and control derivatives from flight test data [2]. Also, a rigid-body formulation of the inertia tensor is essential in the study of aeroelasticity of non-rigid-body aircraft [3, 4]. Thus, the inertia tensor is critical to understanding the flight dynamics of a given aircraft.

The inertia of a completed aircraft can be measured through experimental procedures. The inertia of the aircraft about the principal axes can be measured by suspending or supporting the aircraft in various orientations using varying setups. Several methods have been implemented on aircraft to determine their moments of inertia such as bifilar pendulums [5–9], trifilar pendulums [10], compound pendulums [8, 11, 12], suspension systems [13–15], knife-edge fulcrums [2, 16], torque frames [17], and flight test data [18]. Some studies have found the accuracy of different methods to be axis dependant [2]. While the majority of these methods can be used to provide accurate results, an estimate of the aircraft inertia tensor is frequently desired in the early stages of design, prior to building the aircraft.

Inertial estimates are crucial to the preliminary design phase of an aircraft. These estimates are used not only for control surface sizing and design rules, but also for designing the control system per maneuverability requirements [1]. Numerical methods are an appropriate tool for calculating the inertia of an aircraft under design. One method involves modeling the internal structure of an aircraft in a computer-aided design (CAD) package, and thus determining the inertia through a finite element mass analysis [19–22]. Another method that has been used is the lumped masses method. This method involves discretizing the aircraft into small spherical masses of variable size and constant density to approximate the mass and inertia distribution throughout the aircraft [19, 23–25]. These methods are incredibly useful. However, such methods are complex and generally expensive in computational resources. Both methods also require an extensive knowledge of the weight distribution within the design. Another method uses statistical data of aircraft radii of gyration to predict the inertia about the principal axes [19]. One downside to this method is the need for a complex and comprehensive database of aircraft properties. Such complex methods can be difficult to implement correctly and precisely.

The method presented and discussed in the present paper is a step toward simplifying aircraft inertial calculations with improved accuracy and precision. We propose that the moments and products of inertia of an aircraft can be estimated using a series of components including rectangular cuboids, cylinders, spheres, wing segments, and rotors. The method for calculating the mass and inertial properties of a wing presented and discussed in the present paper is similar to that presented by Lanham [1], with fewer assumptions. The closed-form equations for the calculations of the inertia of each component is presented, along with the method of summing their influences to obtain an estimate for the inertial properties of the complete aircraft based on component position and orientation.

III. Generalized Mass Properties

In the present work, we will assume that the complete aircraft consists of a finite number of objects called components, each of which has constant density.

A. Volume, Mass, and Weight

The total volume of an object can be found by integrating the region within the geometry. This can be written as a volume integral

$$V = \iiint_V dV \tag{1}$$

The mass of an object of constant density is simply

$$m = \rho V \tag{2}$$

and the weight W of an object is

$$W = mg \tag{3}$$

where g is the gravitational constant. Because we are assuming constant density, the mass properties of an object can be completely defined by the volume, and either the mass, density, or weight of the object.

B. Center of Gravity

The center of gravity (CG) location of an object can be determined from the mass distribution. For an object with constant density, the moments along each axis can be written as the volume integrals

$$M_{yz} = \rho \iiint_V x \, dV \tag{4}$$

$$M_{xz} = \rho \iiint_V y \, dV \tag{5}$$

$$M_{xy} = \rho \iiint_V z \, dV \tag{6}$$

The coordinates of the object CG relative to the object origin can then be computed from

$$\bar{x} \equiv \frac{M_{yz}}{m} \tag{7}$$

$$\bar{y} \equiv \frac{M_{xz}}{m} \tag{8}$$

$$\bar{z} \equiv \frac{M_{xy}}{m} \tag{9}$$

C. Mass Moment of Inertia

The mass moment of inertia of an object can be expressed in tensor form as

$$[\mathbf{I}] = \begin{bmatrix} I_{xx} & -I_{xy} & -I_{xz} \\ -I_{yx} & I_{yy} & -I_{yz} \\ -I_{zx} & -I_{zy} & I_{zz} \end{bmatrix} \tag{10}$$

where the individual moments and products of inertia for an object of constant density can be computed from the volume integrals

$$I_{xx} = \rho \iiint_V (y^2 + z^2)\, dV \tag{11}$$

$$I_{yy} = \rho \iiint_V (x^2 + z^2)\, dV \tag{12}$$

$$I_{zz} = \rho \iiint_V (x^2 + y^2)\, dV \tag{13}$$

$$I_{xy} = I_{yx} = \rho \iiint_V (xy)\, dV \tag{14}$$

$$I_{xz} = I_{zx} = \rho \iiint_V (xz)\, dV \tag{15}$$

$$I_{yz} = I_{zy} = \rho \iiint_V (yz)\, dV \tag{16}$$

In the present work we will refer to the mass moment of inertia as simply the *moment of inertia*. We will now consider how these generalized mass properties can be used to evaluate the mass properties of a complete aircraft composed of a finite number of individual components of constant density.

IV. Component Properties

The mass and moment-of-inertia properties of a complete aircraft can be estimated by summing the influences of the individual components that make up the complete aircraft. Here we include common simple geometries that can be used to model the mass properties of many aircraft components. Additionally, estimates for more complex geometries such as wings and rotors are also included. We begin here with the more simple geometries and progress to the complex. In all cases, we assume that each component is a solid of constant density. Note that for the simple geometries, detailed derivations of the required integrals are not included, since these are widely known and can be found in many text books [26, 27]. However, the integrations required for the wing and rotor estimates are included here for completeness.

A. Rectangular Cuboid

A cuboid is a solid with six faces, or hexahedron. Here we consider a rectangular cuboid, which is a cuboid for which all faces are rectangles, and all neighboring faces meet at right angles. The center of gravity of a rectangular cuboid is located at the center of the object. We define a Cartesian coordinate system such that the origin lies at the object CG and each axis is parallel or perpendicular to the cuboid faces. The cuboid size is defined by a length of the cuboid along each axis, as shown in Fig. 1.

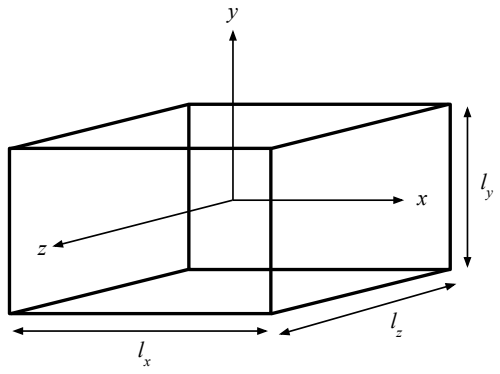

Fig. 1 Rectangular cuboid geometric definition and coordinate system.

The volume of the rectangular cuboid is obtained from the integral

$$V \equiv \iiint_V dV = \int_{-l_z/2}^{l_z/2} \int_{-l_y/2}^{l_y/2} \int_{-l_x/2}^{l_x/2} dx dy dz = l_x l_y l_z \tag{17}$$

Using these same limits of integration in Eqs. (11) – (16), performing the integration, and applying the result to Eq. (10) gives the inertia tensor for a rectangular cuboid computed about the origin of the cuboid

$$[\mathbf{I}] = \begin{bmatrix} \frac{m}{12}(l_y^2 + l_z^2) & 0 & 0 \\ 0 & \frac{m}{12}(l_x^2 + l_z^2) & 0 \\ 0 & 0 & \frac{m}{12}(l_x^2 + l_y^2) \end{bmatrix} \tag{18}$$

For the case of a hollow rectangular cuboid with inner dimensions l_{x1}, l_{y1}, l_{z1} and outer dimensions l_{x2}, l_{y2}, l_{z2}, it can be shown that the volume is

$$V = V_2 - V_1 \tag{19}$$

where $V_1 = l_{x1} l_{y1} l_{z1}$ and $V_2 = l_{x2} l_{y2} l_{z2}$. The inertia tensor about the origin is

$$[\mathbf{I}] = \begin{bmatrix} \frac{m}{12}\frac{V_2(l_{y2}^2+l_{z2}^2)-V_1(l_{y1}^2+l_{z1}^2)}{V_2-V_1} & 0 & 0 \\ 0 & \frac{m}{12}\frac{V_2(l_{x2}^2+l_{z2}^2)-V_1(l_{x1}^2+l_{z1}^2)}{V_2-V_1} & 0 \\ 0 & 0 & \frac{m}{12}\frac{V_2(l_{x2}^2+l_{y2}^2)-V_1(l_{x1}^2+l_{y1}^2)}{V_2-V_1} \end{bmatrix} \tag{20}$$

B. Hollow Cylinder

Consider a hollow cylinder with an inner radius R_1 and outer radius R_2 and having a length h. Here we will define a coordinate system such that the origin is placed at the cylinder center of gravity, and the x axis is aligned with the axis of the cylinder as shown in Fig. 2.

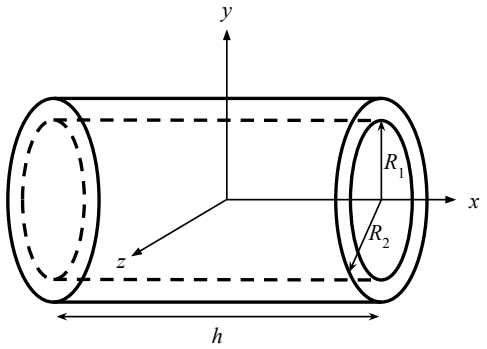

Fig. 2 Cylinder geometric definition and coordinate system.

The volume integrals required for Eqs. (1) and (11)–(16) are most easily carried out in cylindrical coordinates (x, r, φ) where $r = y^2 + z^2$. The volume can be obtained from the integral

$$V \equiv \iiint_V dV = \int_0^{2\pi} \int_{R_1}^{R_2} \int_{-h/2}^{h/2} dx r dr d\varphi = \pi h (R_2^2 - R_1^2) \tag{21}$$

The inertia tensor relative to the component origin is

$$[\mathbf{I}] = \begin{bmatrix} \frac{m}{2}(R_2^2 + R_1^2) & 0 & 0 \\ 0 & \frac{m}{12}[3(R_2^2 + R_1^2) + h^2] & 0 \\ 0 & 0 & \frac{m}{12}[3(R_2^2 + R_1^2) + h^2] \end{bmatrix} \tag{22}$$

The case of a solid cylinder can be computed by simply setting $R_1 = 0$.

C. Hollow Sphere

Consider a hollow sphere with an inner radius R_1 and outer radius R_2as shown in Fig. 3.

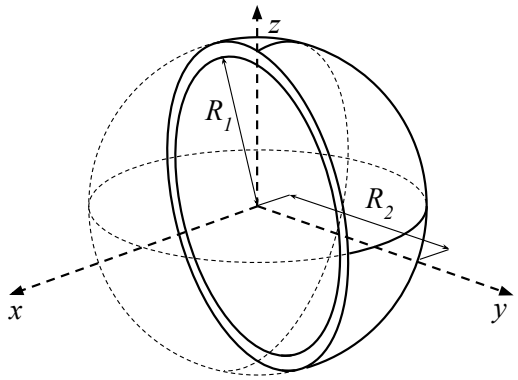

Fig. 3 Sphere geometric definition and coordinate system.

The origin is placed at the sphere center of gravity, which, for a sphere of constant density, is at the center of the sphere. Recognizing that the surface area of a sphere is $4\pi r^2$, the volume of the sphere can be obtained from the integral

$$V \equiv \iiint_V dV = \int_{R_1}^{R_2} 4\pi r^2 dr = \frac{4}{3}\pi(R_2^3 - R_1^3) \tag{23}$$

The moment of inertia of the sphere about the object origin is

$$[\mathbf{I}] = \begin{bmatrix} \frac{2}{5}m\frac{(R_2^5-R_1^5)}{(R_2^3-R_1^3)} & 0 & 0 \\ 0 & \frac{2}{5}m\frac{(R_2^5-R_1^5)}{(R_2^3-R_1^3)} & 0 \\ 0 & 0 & \frac{2}{5}m\frac{(R_2^5-R_1^5)}{(R_2^3-R_1^3)} \end{bmatrix} \tag{24}$$

The case of a solid sphere can be computed by simply setting $R_1 = 0$.

D. Wing Segment

To estimate the mass and inertia properties of a finite wing, we will assume that any lifting surface can be divided into a finite number of simple wing segments. We will assume that more complex wing geometries can be approximated by combining a number of simple wing segments. Therefore, here we present a method for approximating the volume, mass, and inertial properties of a single segment. For more complex wings, this process can be repeated for each wing segment and the results summed, similar to summing the influences of any number of components on the aircraft.

1. Geometry and Coordinate Definitions

Each wing segment can be defined by the span b, root chord c_r, tip chord c_t, root airfoil thickness τ_r, tip airfoil thickness τ_t, airfoil thickness distribution, sweep angle Λ, and dihedral angle Γ. For any given wing segment, the sweep and dihedral angles are assumed to be constant, and the chord and airfoil thickness are assumed to change linearly as a function of spanwise location. In this development, we will neglect the influence of wing twist, since twist generally has very little affect on the mass properties of the wing relative to the other parameters listed.

The geometries discussed in the forgoing sections were all simple geometries, of which the location of the center of gravity was known for each object due to the symmetry of each geometry. Hence, the origin for each object was easily defined at the center of gravity. For the case of a finite wing, we shall define a coordinate system that is not coincident with the wing center of gravity, since the center of gravity of the wing is not known a priori.

In the present analysis, we shall use the coordinate system for a wing segment as defined in Fig. 4. The origin of the coordinate frame is placed at the wing-root quarter-chord. The x-axis follows the chord-line pointing out the root

leading edge, the y-axis in the direction of a right wing, and the z-axis points out the bottom, orthogonal to both the x and y axes.

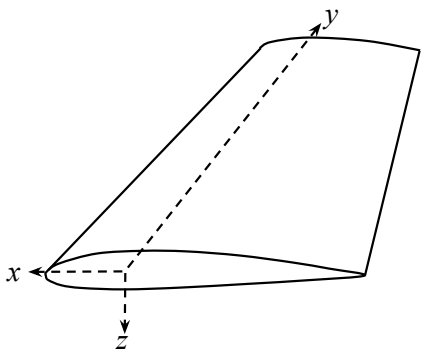

Fig. 4 Drawing of the wing-segment coordinate frame.

Wing sweep is defined as a chordwise shearing of the wing in the xy plane as shown in Fig. 5. A positive sweep angle moves the wing tip aft, and a negative sweep angle moves the wing tip forward. The sweep angle is the angle between the y-axis and a line connecting the root and tip quarter-chords, as shown in Fig. 5.

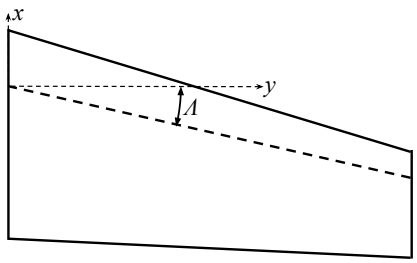

Fig. 5 Quarter chord sweep angle.

Wing dihedral is defined as a rotation of the wing about the aircraft x axis as shown in Fig. 6. A positive dihedral angle moves the wing tip up relative to the wing root, and a negative dihedral (i.e. anhedral) angle moves the wingtip down relative to the wing root. Note that the dihedral angle is not defined with respect to the wing-segment coordinate frame, but rather the aircraft coordinate frame. Dihedral represents a rotation of the wing coordinate frame relative to the aircraft coordinate frame. This distinction is made because the wing-segment coordinate frame will later be rotated by the dihedral angle and shifted within the aircraft coordinate frame. Therefore, effects of dihedral will not be included in the wing mass and inertia properties, but will be included once the inertia on the complete aircraft is considered.

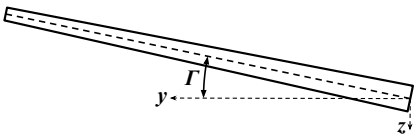

Fig. 6 Dihedral is a rotation of the wing coordinate system about the aircraft coordinate frame x axis.

Here we will allow the chord c and airfoil maximum thickness in percent chord τ_m to vary linearly from root to tip of the wing segment

$$c(y) = (c_t - c_r)\frac{y}{b} + c_r \tag{25}$$

$$\tau_m(y) = (\tau_t - \tau_r)\frac{y}{b} + \tau_r \tag{26}$$

The maximum wing thickness at any spanwise location depends on both the local airfoil maximum thickness and the local chord according to

$$t_m(y) = \tau_m(y)c(y) \tag{27}$$

Note that since both $\tau_m(y)$ and $c(y)$ are allowed to vary linearly, $t(y)$ may be nonlinear.

The airfoil used for the wing segment can have a significant affect on the mass properties of the wing. We will assume that the mass properties of the airfoil are dominated by the airfoil thickness distribution, and that effects of camber are negligible. For the purposes of this analysis, it is helpful to define an airfoil coordinate system. Here we use the traditional coordinate frame for an airfoil, with the x-axis pointing along the chord-line out the trailing edge, and the y-axis pointing up normal to the x-axis. The ordinates are subscripted as x_a and y_a for clarity. This is shown below in Fig. 7.

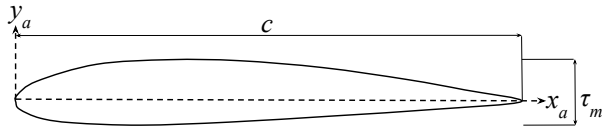

Fig. 7 Airfoil coordinate frame.

The thickness distribution of an airfoil as a function of percent chord $\tau(x_a/c)$ can be defined as the product of the maximum thickness τ_m and thickness distribution function $\mu(x_a/c)$

$$\tau\left(\frac{x_a}{c}\right) = \tau_m \mu\left(\frac{x_a}{c}\right) \tag{28}$$

In the present analysis, we will assume that the thickness distribution function $\mu(x_a/c)$ is constant across the wing segment, although the maximum thickness τ_m is allowed to vary linearly as shown in Eq. (26). The method presented here can be used to account for any arbitrary thickness distribution $\mu(x_a/c)$. Results for two thickness distributions will be included as examples, but the process can be repeated for other thickness distributions. The two thickness distributions that will be considered here are the NACA 4-digit series distribution, and a diamond airfoil distribution. The thickness distribution of the NACA 4-digit series [28] can be written as

$$\mu\left(\frac{x_a}{c}\right) = a_0\sqrt{\frac{x_a}{c}} + a_1\left(\frac{x_a}{c}\right) + a_2\left(\frac{x_a}{c}\right)^2 + a_3\left(\frac{x_a}{c}\right)^3 + a_4\left(\frac{x_a}{c}\right)^4 \tag{29}$$

In the present analysis, we shall present results in terms of the five coefficients needed to define the thickness distribution in Eq. (29). This thickness distribution is quite versatile, and can be used to fit a wide range of airfoils outside of the NACA 4-digit series. Any values for these coefficients can be used without loss of generality of the model. Table 1 shows values for each of these coefficients that can be used to match the thickness distribution for a number of airfoils, even those that do not use a NACA 4-digit thickness distribution.

Table 1 NACA 4-digit series coefficients for various airfoil thickness distributions.

Airfoil	a_0	a_1	a_2	a_3	a_4
Traditional NACA 4-Digit Series	2.969	-1.260	-3.516	2.843	-1.015
NACA 4-Digit Series with closed trailing edge [29]	2.980	-1.320	-3.286	2.441	-0.815
Clark Y (with $\tau_m = 0.117$)	2.947	-1.102	-3.975	3.533	-1.399
Selig S1010	0.0001	9.998	0.087	-1.922	14.381
Diamond with τ_m at $x/c = 0.5$	0.479	-0.948	14.248	-26.970	13.234

The general thickness distribution for a diamond airfoil will also be demonstrated. This thickness distribution can be written as

$$\mu\left(\frac{x_a}{c}\right) = \begin{cases} \frac{x_a/c}{x_m/c}, & 0 \le \frac{x_a}{c} \le \frac{x_m}{c} \\ \frac{1-x_a/c}{1-x_m/c}, & \frac{x_m}{c} \le \frac{x_a}{c} \le 1 \end{cases} \tag{30}$$

where x_m/c is the chordwise location of max thickness in percent chord.

With these definitions in mind, a wing segment can be fully defined by the span b, root chord c_r, tip chord c_t, root airfoil thickness τ_r, tip airfoil thickness τ_t, sweep angle Λ, dihedral angle Γ, and airfoil thickness distribution $\mu(x_a/c)$. Figure 8 shows a single wing segment with the geometric parameters included. Note that the span length b is defined parallel to the y-axis.

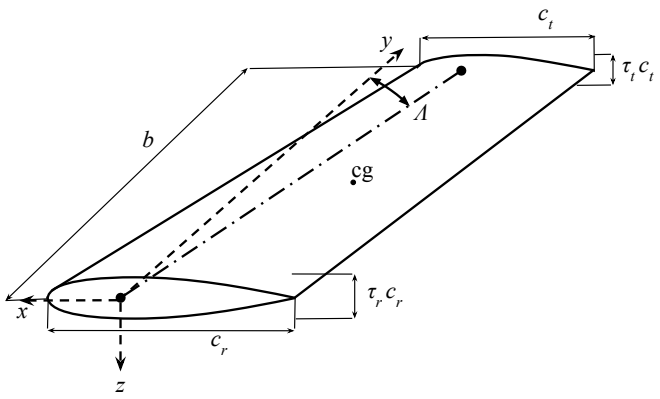

Fig. 8 Wing-segment geometry definitions.

2. Volume and Center of Gravity

The mass and inertial properties of the wing require solving the integrals given in Eqs. (1), (4)–(6), and (11)–(16). Each of these integrals are volume integrals with terms of the form $x^i y^j z^k$ where i, j, and k are each positive integers. For brevity within the body of this manuscript, detailed solutions to those integrals are not included here, but are included in Appendix A. Their solutions will be referenced here as $S_{i,j,k}$. Integrals related to the airfoil thickness distribution are included in Appendix C.

The volume of a wing is bounded in the wing-segment coordinate frame by the region

$$0 \leq \hat{x} \leq 1 \tag{31}$$

$$0 \leq \hat{y} \leq 1 \tag{32}$$

$$0 \leq \hat{z} \leq 1 \tag{33}$$

where the change of variables

$$\hat{x} = \frac{1}{4} - \frac{x}{c(\hat{y})} \tag{34}$$

$$\hat{y} = \frac{y}{b} \tag{35}$$

$$\hat{z} = \frac{1}{2} - \frac{z}{\tau_m(\hat{y})\mu(\hat{x})c(\hat{y})} \tag{36}$$

has been applied. This change of variables results in the derivatives

$$d\hat{x} = -\frac{dx}{c(\hat{y})} \tag{37}$$

$$d\hat{y} = \frac{dy}{b} \tag{38}$$

$$d\hat{z} = -\frac{dz}{\tau_m(\hat{y})\mu(\hat{x})c(\hat{y})} \tag{39}$$

Note that the negative signs in the derivatives for x and z are used in the appendical derivations to flip the integrand direction from 1 through 0 to 0 through 1, as shown here.

The local chord and maximum airfoil thickness given in Eqs. (25) and (26) can be written using this change of variables as

$$c(\hat{y}) = (c_t - c_r)\,\hat{y} + c_r \tag{40}$$

$$\tau_m(\hat{y}) = (\tau_t - \tau_r)\,\hat{y} + \tau_r \tag{41}$$

Because the dimensional x and $c(\hat{y})$ values in Eq. (34) are in the wing segment coordinate system, the symbol $\hat{x}$ is equivalent to the local airfoil chordwise ratio x_a/c. Therefore, the general thickness distribution given in Eq. (28) can be written as a function of both spanwise location and chordwise coordinate

$$\tau(\hat{x}, \hat{y}) = \tau_m(\hat{y})\mu(\hat{x}) \tag{42}$$

For the NACA 4-digit thickness distribution

$$\mu(\hat{x}) = a_0\sqrt{\hat{x}} + a_1\hat{x} + a_2\hat{x}^2 + a_3\hat{x}^3 + a_4\hat{x}^4 \tag{43}$$

and for the diamond airfoil thickness distribution

$$\mu(\hat{x}) = \begin{cases} \frac{\hat{x}}{\hat{x}_m}, & 0 \le \hat{x} \le \hat{x}_m \\ \frac{1-\hat{x}}{1-\hat{x}_m}, & \hat{x}_m \le \hat{x} \le 1 \end{cases} \tag{44}$$

Due to our definition of thickness distribution in the chordwise direction, the z bounds depend on the chordwise coordinate x. Also, due to our definition of linear changes in chord and airfoil thickness, the x and z bounds depend on the spanwise coordinate y. Using these bounds in Eq. (1) and integrating, we find the volume of the wing segment to be

$$V = S_{0,0,0} = \frac{b}{12}\kappa_a \upsilon_0 \tag{45}$$

where

$$\kappa_a \equiv \tau_r\left(3c_r^2 + 2c_r c_t + c_t^2\right) + \tau_t\left(c_r^2 + 2c_r c_t + 3c_t^2\right) \tag{46}$$

The parameter υ_0 depends on an integral that is a function of the thickness distribution as shown in Eqs. (C.1) - (C.4). For a wing using the NACA 4-digit thickness distribution,

$$\upsilon_0 = \frac{1}{60}\left(40a_0 + 30a_1 + 20a_2 + 15a_3 + 12a_4\right) \tag{47}$$

and for a wing using the diamond airfoil thickness distribution,

$$\upsilon_0 = \frac{1}{2} \tag{48}$$

A detailed derivation of the integrals resulting in the expressions for κ_a and υ_0 are included in Appendices A and C.

In order to compute the wing segment center of gravity, the volume integrals given in Eqs. (4)–(6) must be computed. Because sweep affects the x coordinate of the mass of the wing, the sweep angle must be accounted for in the computation of M_{yz}. To compute the moment M_{yz}, the shift $-y\tan\Lambda$ due to sweep can be applied to the x coordinate, which gives

$$M_{yz} = \rho \iiint_V (x - y\tan\Lambda)\; dV = \rho \iiint_V x\, dV - \rho\tan\Lambda \iiint_V y\, dV \tag{49}$$

It should be noted that sweep does not need to be applied to the integrations for M_{xz} or M_{xy} in Eqs. (5) and (6) because these integrals do not contain an x term, and because sweep does not affect the y or z coordinates of mass within the wing segment. Because sweep affects a right wing differently than a left wing, we will account for the difference in solution between left and right wings by defining

$$\delta \equiv \begin{cases} 1, & \text{right wing} \\ -1, & \text{left wing} \end{cases} \tag{50}$$

The integrals required to find M_{yz}, M_{xy}, and M_{xz} about the wing root quarter-chord are given in Appendix A, and result in

$$M_{yz} = \rho[S_{1,0,0} - \tan\Lambda S_{0,1,0}] = -\rho\frac{b}{240}\left[3\kappa_b\upsilon_1 + 4b\kappa_c\upsilon_0\tan\Lambda\right] \tag{51}$$

$$M_{xz} = \rho\delta S_{0,1,0} = \rho\delta\frac{b^2}{60}\kappa_c\upsilon_0 \tag{52}$$

$$M_{xy} = \rho S_{0,0,1} = 0 \tag{53}$$

where

$$\kappa_b \equiv \tau_r\left(4c_r^3 + 3c_r^2c_t + 2c_rc_t^2 + c_t^3\right) + \tau_t\left(c_r^3 + 2c_r^2c_t + 3c_rc_t^2 + 4c_t^3\right) \tag{54}$$

$$\kappa_c \equiv \tau_r\left(3c_r^2 + 4c_rc_t + 3c_t^2\right) + 2\tau_t\left(c_r^2 + 3c_rc_t + 6c_t^2\right) \tag{55}$$

For a wing using the NACA 4-digit thickness distribution,

$$\upsilon_1 = \frac{1}{60}\left(56a_0 + 50a_1 + 40a_2 + 33a_3 + 28a_4\right) \tag{56}$$

and for a wing using the diamond airfoil thickness distribution,

$$\upsilon_1 = \frac{4\hat{x}_{mt} + 1}{6} \tag{57}$$

Using Eq. (45) in Eq. (2), and applying the result along with Eqs. (51)–(53) in Eqs. (7) – (9) gives the location of the center of gravity relative to the wing origin

$$\bar{x} \equiv \frac{M_{yz}}{m} = -\frac{3\kappa_b\upsilon_1 + 4b\kappa_c\upsilon_0\tan\Lambda}{20\kappa_a\upsilon_0} \tag{58}$$

$$\bar{y} \equiv \frac{M_{xz}}{m} = \delta b\frac{\kappa_c}{5\kappa_a} \tag{59}$$

$$\bar{z} \equiv \frac{M_{xy}}{m} = 0 \tag{60}$$

As can be expected, because we neglect twist and camber, the z coordinate of the CG is zero. Also note that, as one might expect, sweep only affects the x coordinate of the CG.

3. Inertia Tensor

The inertia tensor for the wing segment can be computed about the origin of the wing-segement coordinate system shown in Fig. 8 using the volume integrals given in Eqs. (11)–(16) with appropriate limits. Applying the shift due to sweep gives the inertia tensor about the wing segment origin

$$[\mathbf{I}]_o = \rho\iiint_V \begin{bmatrix} y^2+z^2 & -(xy) & -(xz) \\ -(xy) & x^2+z^2 & -(yz) \\ -(xz) & -(yz) & x^2+y^2 \end{bmatrix} dV + \rho\iiint_V \begin{bmatrix} 0 & -(-y^2\tan\Lambda) & -(-yz\tan\Lambda) \\ -(-y^2\tan\Lambda) & y^2\tan^2\Lambda - 2xy\tan\Lambda & 0 \\ -(-yz\tan\Lambda) & 0 & y^2\tan^2\Lambda - 2xy\tan\Lambda \end{bmatrix} dV \tag{61}$$

The volume integrals required in Eq. (61) are included in Appendix A, and result in

$$[\mathbf{I}]_o = \begin{bmatrix} I_{xx_o} & -I_{xy_o} & -I_{xz_o} \\ -I_{yx_o} & I_{yy_o} & -I_{yz_o} \\ -I_{zx_o} & -I_{zy_o} & I_{zz_o} \end{bmatrix} \tag{62}$$

where

$$I_{xx_o} = \rho(S_{0,2,0} + S_{0,0,2}) = \rho\frac{b}{3360}\left(56b^2\kappa_f\upsilon_0 + \kappa_g\upsilon_3\right) \tag{63}$$

$$\begin{aligned} I_{yy_o} &= \rho(S_{2,0,0} + S_{0,0,2} + S_{0,2,0}\tan^2\Lambda - 2S_{1,1,0}\tan\Lambda) \\ &= \rho\frac{b}{10080}\left[84b\left(2b\kappa_f\tan^2\Lambda + \kappa_d\tan\Lambda\right)\upsilon_1 + 49\kappa_e\upsilon_2 + 3\kappa_g\upsilon_3\right] \end{aligned} \tag{64}$$

$$\begin{aligned} I_{zz_o} &= \rho\left[S_{2,0,0} + \left(\tan^2\Lambda + 1\right)S_{0,2,0} - 2S_{1,1,0}\tan\Lambda\right] \\ &= \rho\frac{b}{1440}\left[12b\left\{2b\left(\tan^2\Lambda + 1\right)\kappa_f\upsilon_0 + \kappa_d\upsilon_1\tan\Lambda\right\} + 7\kappa_e\upsilon_2\right] \end{aligned} \tag{65}$$

$$I_{xy_o} = I_{yx_o} = \rho\delta(S_{1,1,0} - S_{0,2,0}\tan\Lambda) = -\rho\delta\frac{b^2}{240}\left[4b\kappa_f\upsilon_0\tan\Lambda + \kappa_d\upsilon_1\right] \tag{66}$$

$$I_{xz_o} = I_{zx_o} = \rho(S_{1,0,1} - S_{0,1,1}\tan\Lambda) = 0 \tag{67}$$

$$I_{yz_o} = I_{zy_o} = \rho\delta S_{0,1,1} = 0 \tag{68}$$

and

$$\kappa_d \equiv \tau_r\left(c_r + c_t\right)\left(2c_r^2 + c_rc_t + 2c_t^2\right) + \tau_t\left(c_r^3 + 3c_r^2c_t + 6c_rc_t^2 + 10c_t^3\right) \tag{69}$$

$$\kappa_e \equiv \tau_r\left(5c_r^4 + 4c_r^3c_t + 3c_r^2c_t^2 + 2c_rc_t^3 + c_t^4\right) + \tau_t\left(c_r^4 + 2c_r^3c_t + 3c_r^2c_t^2 + 4c_rc_t^3 + 5c_t^4\right) \tag{70}$$

$$\kappa_f \equiv \tau_r\left(c_r^2 + 2c_rc_t + 2c_t^2\right) + \tau_t\left(c_r^2 + 4c_rc_t + 10c_t^2\right) \tag{71}$$

$$\begin{aligned} \kappa_g \equiv\ & \tau_r^3\left(35c_r^4 + 20c_r^3c_t + 10c_r^2c_t^2 + 4c_rc_t^3 + c_t^4\right) + \tau_r^2\tau_t\left(15c_r^4 + 20c_r^3c_t + 18c_r^2c_t^2 + 12c_rc_t^3 + 5c_t^4\right) \\ & + \tau_r\tau_t^2\left(5c_r^4 + 12c_r^3c_t + 18c_r^2c_t^2 + 20c_rc_t^3 + 15c_t^4\right) + \tau_t^3\left(c_r^4 + 4c_r^3c_t + 10c_r^2c_t^2 + 20c_rc_t^3 + 35c_t^4\right) \end{aligned} \tag{72}$$

For a wing using the NACA 4-digit thickness distribution,

$$\upsilon_2 = \frac{1}{980}\left(856a_0 + 770a_1 + 644a_2 + 553a_3 + 484a_4\right) \tag{73}$$

$$\begin{aligned} \upsilon_3 = {} & \frac{2}{5}a_0^3 + a_0^2a_1 + \frac{3}{4}a_0^2a_2 + \frac{3}{5}a_0^2a_3 + \frac{1}{2}a_0^2a_4 + \frac{6}{7}a_0a_1^2 + \frac{4}{3}a_0a_1a_2 + \frac{12}{11}a_0a_1a_3 + \frac{12}{13}a_0a_1a_4 \\ & + \frac{6}{11}a_0a_2^2 + \frac{12}{13}a_0a_2a_3 + \frac{4}{5}a_0a_2a_4 + \frac{2}{5}a_0a_3^2 + \frac{12}{17}a_0a_3a_4 + \frac{6}{19}a_0a_4^2 + \frac{1}{4}a_1^3 + \frac{3}{5}a_1^2a_2 \\ & + \frac{1}{2}a_1^2a_3 + \frac{3}{7}a_1^2a_4 + \frac{1}{2}a_1a_2^2 + \frac{6}{7}a_1a_2a_3 + \frac{3}{4}a_1a_2a_4 + \frac{3}{8}a_1a_3^2 + \frac{2}{3}a_1a_3a_4 + \frac{3}{10}a_1a_4^2 \\ & + \frac{1}{7}a_2^3 + \frac{3}{8}a_2^2a_3 + \frac{1}{3}a_2^2a_4 + \frac{1}{3}a_2a_3^2 + \frac{3}{5}a_2a_3a_4 + \frac{3}{11}a_2a_4^2 + \frac{1}{10}a_3^3 + \frac{3}{11}a_3^2a_4 + \frac{1}{4}a_3a_4^2 + \frac{1}{13}a_4^3 \end{aligned} \tag{74}$$

and for a wing using the diamond airfoil thickness distribution,

$$\upsilon_2 = \frac{8\hat{x}_{mt}^2 + 3}{14} \tag{75}$$

$$\upsilon_3 = \frac{1}{4} \tag{76}$$

Because the mass is related to the volume and density according to Eq. (2), applying Eq. (2) along with the relation

for volume given in Eq. (45) gives the tensor components in terms of mass rather than density

$$I_{xx_o} = m\left[\frac{56b^2\kappa_f\upsilon_0 + \kappa_g\upsilon_3}{280\kappa_a\upsilon_0}\right] \tag{77}$$

$$I_{yy_o} = m\left[\frac{84b\left(2b\kappa_f\upsilon_0\tan^2\Lambda + \kappa_d\upsilon_1\tan\Lambda\right) + 49\kappa_e\upsilon_2 + 3\kappa_g\upsilon_3}{840\kappa_a\upsilon_0}\right] \tag{78}$$

$$I_{zz_o} = m\left[\frac{12b\left\{2b\left(\tan^2\Lambda + 1\right)\kappa_f\upsilon_0 + \kappa_d\upsilon_1\tan\Lambda\right\} + 7\kappa_e\upsilon_2}{120\kappa_a\upsilon_0}\right] \tag{79}$$

$$I_{xy_o} = I_{yx_o} = -\delta bm\left[\frac{4b\kappa_f\upsilon_0\tan\Lambda + \kappa_d\upsilon_1}{20\kappa_a\upsilon_0}\right] \tag{80}$$

$$I_{xz_o} = I_{zx_o} = I_{yz_o} = I_{zy_o} = 0 \tag{81}$$

The κ parameters included in this derivation depend on integrals based on the assumption that the wing segment varies linearly in chord and thickness distribution. Detailed derivations for these integrals is included in Appendix A. The υ parameters included in this derivation come from integrals that depend on the thickness distribution. Example solutions for the NACA 4-digit series and diamond airfoil thickness distributions are included here. Detailed integration steps for these parameters are included in Appendix B. Although we have included results here for only two thickness distributions, the integrals for any airfoil thickness distribution can be easily carried out by following the steps shown in Appendix B.

The inertia components given in Eqs. (63)–(68) and (77)–(81) can be used in Eq. (62) to compute the inertia tensor about the origin of the wing-segment coordinate frame. However, in order to include the inertial components of the wing segment in the computation of the inertia of the entire aircraft, it is helpful to know the inertial components of the wing segment about the CG of the wing segment. From the parallel axis theorem, the inertia tensor about an arbitrary point $[\mathbf{I}]_1$ is related to the inertia tensor about the center of gravity $[\mathbf{I}]$ according to

$$[\mathbf{I}]_1 = [\mathbf{I}] + m\left[(\mathbf{s}\cdot\mathbf{s})[\mathbf{E}] - \mathbf{s}\mathbf{s}^T\right] \tag{82}$$

where s is the vector from the center of gravity to the point of interest and $[\mathbf{E}]$ is a 3×3 identity matrix. This relationship can be rearranged to yield the inertia about the wing-segment CG given the inertia about the origin of the wing-segment coordinate system

$$[\mathbf{I}] = [\mathbf{I}]_o - m\left[(\mathbf{s}\cdot\mathbf{s})[\mathbf{E}] - \mathbf{s}\mathbf{s}^T\right] \tag{83}$$

where $\mathbf{s}$ is the vector from the wing-segment CG to the wing-segment origin

$$\mathbf{s} = -\begin{Bmatrix}\bar{x}\\ \bar{y}\\ \bar{z}\end{Bmatrix} \tag{84}$$

For any given wing segment, $\mathbf{s}$ can be computed from Eqs. (58)–(60). Using Eq. (84) in Eq. (83) and simplifying gives the inertia tensor of the wing segment about the wing segment CG

$$[\mathbf{I}] = [\mathbf{I}]_o - m\begin{bmatrix}\bar{y}^2+\bar{z}^2 & -\bar{x}\bar{y} & -\bar{x}\bar{z}\\ -\bar{x}\bar{y} & \bar{x}^2+\bar{z}^2 & -\bar{y}\bar{z}\\ -\bar{x}\bar{z} & -\bar{y}\bar{z} & \bar{x}^2+\bar{y}^2\end{bmatrix} \tag{85}$$

E. Rotor

Several types of rotors are commonly used on aircraft. These include propellers, jet engines, helicopter rotor blades, and others. To estimate the mass and inertial properties of a rotor, we will assume that the rotor can be defined by the number of blades N_b, rotor diameter d_r, hub diameter d_h, hub height h_h, blade root chord c_r, blade tip chord c_t, blade root airfoil thickness τ_r, and blade tip airfoil thickness τ_t. Just as we neglected wing twist and airfoil camber in the analysis of a wing segment, we will neglect the influence of blade pitch and airfoil camber in the present analysis. Figure

9 shows a rotor and the associated local Cartesian coordinates. Note that, because camber and pitch are neglected, the coordinate system of the origin is also the rotor center of gravity.

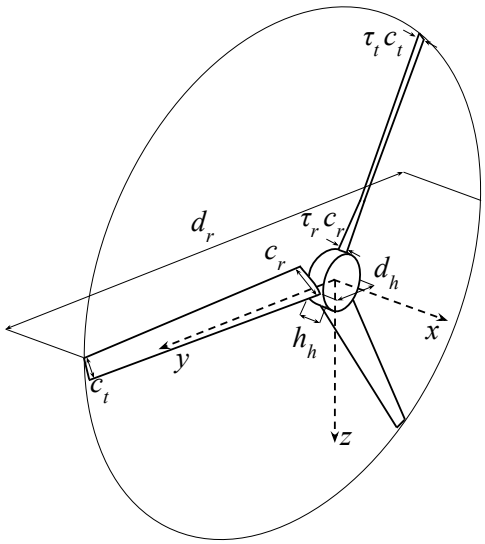

Fig. 9 Rotor geometry definitions.

Here we will use the symbols $r_r = d_h/2$ and $r_t = d_r/2$ to be the radius at the blade root and tip respectively. We will assume that the chord and maximum airfoil thickness ratio vary linearly as a function of radius r according to

$$c(r) = (c_t - c_r)\frac{(r - r_r)}{(r_t - r_r)} + c_r \tag{86}$$

$$\tau_m(r) = (\tau_t - \tau_r)\frac{(r - r_r)}{(r_t - r_r)} + \tau_r \tag{87}$$

Hence, the dimensional maximum airfoil thickness at any radius is

$$t(r) = \tau_m(r)c(r) \tag{88}$$

1. Volume

The volume of the rotor can be estimated by summing the volume of each blade with the volume of the hub. The volume of the hub can be estimated as the volume of a cylinder with a diameter equal to the hub diameter, and a height equal to the hub height. Hence, the volume of the hub can be computed from

$$V_h = \pi h_h r_r^2 \tag{89}$$

The volume of an individual rotor blade can be estimated the same way the volume of a wing segment was estimated in the previous section. Replacing the span in Eq. (45) with the difference in rotor radius and hub radius gives

$$V_b = \frac{r_t - r_r}{12}\kappa_a \upsilon_0 \tag{90}$$

The total volume of the rotor is the sum of the volume of the hub and the volume of the blades

$$V = V_h + N_b V_b \tag{91}$$

Given a total weight or mass of the rotor, the density of the rotor can be found by rearranging Eqs. (2) and (3) and applying the total volume estimated from Eq. (91). Once the density is known, the mass and weight of the hub and blades can be found individually from the known individual volumes given in Eqs. (89) and (90). This information will be useful in the computation of the inertia tensor.

2. Inertia Tensor

The inertia tensor of a rotor can be approximated by considering the inertia tensor of the hub and blades independently. The inertia tensor of the hub can be estimated from Eq. (22) by assuming a zero radius for the inner diameter $R_1 = 0$, setting the outer diameter equal to the diameter of the hub $R_2 = r_r$, and using a cylinder height equal to the hub height $h = h_h$. This gives

$$[\mathbf{I}]_h = \begin{bmatrix} \frac{m_h}{2} r_r^2 & 0 & 0 \\ 0 & \frac{m_h}{12}\left(3r_r^2 + h_h^2\right) & 0 \\ 0 & 0 & \frac{m_h}{12}\left(3r_r^2 + h_h^2\right) \end{bmatrix} \tag{92}$$

where m_h is the mass of the hub.

The inertia tensor of the rotor blades at any point in time depends on the orientation of the blades about the axis of the rotor. Since rotors are commonly spinning during flight, the inertia tensor is a function of time. However, an approximate static inertia tensor for the rotor can be developed by distributing the mass of the rotor blades within a circular disk of the same diameter as the rotor. At each radial distance, we will assume the differential volume of the disk is equal to the differential volume from all the rotor blades at the same radial location. This can be done by setting the area of a thin cylinder equal to the area of the rotor blades at any given radial distance. The area of a thin cylinder of radius r and height h is

$$A(r) = 2\pi r h \tag{93}$$

The total area of the rotor blades passing through a given radius is

$$A(r) = N_b \tau_m(r) c(r)^2 \upsilon_0 \tag{94}$$

where $\tau_m \upsilon_0$ accounts for the airfoil area nondimensionalized by c^2. Setting Eq. (93) equal to Eq. (94) and solving for the disk height gives the height of the disk as a function of radial position

$$h(r) = \frac{N_b \tau_m(r) c(r)^2 \upsilon_0}{2\pi r} \tag{95}$$

In order to compute the inertia components, it is helpful to convert this system to polar coordinates (to align the axis as we have defined for the rotor) where

$$\begin{aligned} x &= x \\ y &= r\cos\varphi \\ z &= r\sin\varphi \end{aligned}$$

The angle φ is the angle about the x-axis, with a counter clockwise angle being positive. As we have changed the coordinate system, we will define the inertia in this new polar coordinate frame to be

$$[\mathbf{I}]_b = \rho \iiint_V \begin{bmatrix} r^2 & -(xr\cos\varphi) & -(xr\sin\varphi) \\ -(xr\cos\varphi) & x^2 + r^2\sin^2\varphi & -\left[\frac{1}{2}r^2\sin(2\varphi)\right] \\ -(xr\sin\varphi) & -\left[\frac{1}{2}r^2\sin(2\varphi)\right] & x^2 + r^2\cos^2\varphi \end{bmatrix} dx\, r\, dr\, d\varphi \tag{96}$$

The volume integrals required in Eq. (96) are included in Appendix B, and result in

$$[\mathbf{I}]_b = \begin{bmatrix} I_{xx} & 0 & 0 \\ 0 & I_{yy} & 0 \\ 0 & 0 & I_{zz} \end{bmatrix} \tag{97}$$

where

$$I_{xx} = m_r \frac{T_{0,2,0} + T_{0,0,2}}{T_{0,0,0}} = m_r \left[\frac{r_r^3\gamma_l + r_r^2 r_t \gamma_m + r_r r_t^2 \gamma_n + r_t^3 \gamma_o}{5\left(r_t - r_r\right)\kappa_a}\right] \tag{98}$$

$$I_{yy} = m_r \frac{T_{2,0,0} + T_{0,0,2}}{T_{0,0,0}} = I_{zz} = m_r \frac{T_{2,0,0} + T_{0,2,0}}{T_{0,0,0}} \tag{99}$$

$$I_{xy} = I_{yx} = I_{xz} = I_{zx} = I_{yz} = I_{zy} = 0 \tag{100}$$

with

$$m_r = \rho_r T_{0,0,0} = \frac{1}{12}\rho_r N_b \kappa_a \upsilon_0 \left(r_t - r_r\right) \tag{101}$$

and

$$T_{2,0,0} = N_b^3 \upsilon_0^3 \frac{\gamma_a r_r^{10} + \gamma_b r_r^9 r_t + \gamma_c r_r^8 r_t^2 + \gamma_d r_r^7 r_t^3 + \gamma_e r_r^6 r_t^4 + \gamma_f r_r^5 r_t^5 + \gamma_g r_r^4 r_t^6 + \gamma_h r_r^3 r_t^7 + \gamma_i r_r^2 r_t^8 + \gamma_j r_r r_t^9 + \gamma_k r_t^{10}}{13440\pi^2 r_r r_t (r_r - r_t)^9}$$

$$T_{0,2,0} = T_{0,0,2} = \frac{1}{120} N_b \upsilon_0 \left(r_r^3 \gamma_l + r_r^2 r_t \gamma_m + r_r r_t^2 \gamma_n + r_t^3 \gamma_o\right)$$

The γ values used in the equations above can be found in Appendix B in Eqs. (B.17) – (B.27) and (B.30) – (B.33), and are not reported here in the body of the paper for brevity. Note, the integrations in Appendix B show that $\bar{x} = \bar{y} = \bar{z} = 0$.

The total inertia of the rotor about the origin of the rotor can be computed by summing the inertia of the hub with the inertia of the blades

$$[\mathbf{I}] = [\mathbf{I}]_h + [\mathbf{I}]_b \tag{102}$$

3. Angular Momentum

As a rotor spins, it creates angular momentum that can affect the motion of the aircraft independent of whether the rotor is generating thrust. The angular momentum of the rotor about its own axis of rotation can be computed from the inertia tensor of the rotor and the rotor angular rate. The inertia tensor is given in Eq. (102). Due to our choice of a rotor coordinate system, the angular rate is only about the x axis and can be written in vector form as

$$\omega = \begin{Bmatrix} \omega_x \\ 0 \\ 0 \end{Bmatrix} \tag{103}$$

The angular momentum vector is the product of the inertia tensor and the angular-rate vector, which gives

$$\mathbf{h} = [\mathbf{I}]\omega = [\mathbf{I}] \begin{Bmatrix} \omega_x \\ 0 \\ 0 \end{Bmatrix} = \begin{Bmatrix} I_{xx}\omega_x \\ 0 \\ 0 \end{Bmatrix} \tag{104}$$

Note that this vector is in the component coordinate system. This will be used in a subsequent section to evaluate the angular momentum of the entire aircraft due to spinning rotors.

V. Mass and Inertial Properties of the Complete Aircraft

The mass and inertial properties of the individual components can be used to obtain an estimate for the total mass, center-of-gravity location, and inertia tensor of the entire aircraft. The influence of each component on the global aircraft properties depends on the component position and orientation relative to the aircraft origin and coordinate system.

A. Coordinate Frames

We will use the traditional body-fixed coordinate frame for an aircraft. The x-axis points out the nose, the y-axis out the right wing, and the z-axis points out the bottom, orthogonal to both the x and y axes. This is shown below in Fig. 10. The origin of this coordinate frame is placed at the center of gravity of the aircraft. The inertia tensor of an aircraft is traditionally reported in this coordinate frame.

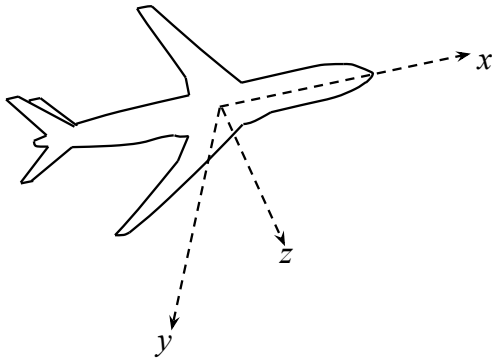

Fig. 10 Drawing of the aircraft coordinate frame.

B. Orientation and Position

1. Orientation

The orientation of each component relative to the aircraft coordinate system can be defined using the traditional Euler angles ϕ, θ, and ψ. Although there are multiple ways to define Euler angles, the Euler angles used in this work will be defined as

$$\begin{aligned} \phi &\equiv \text{Bank Angle} \\ \theta &\equiv \text{Elevation Angle} \\ \psi &\equiv \text{Azimuth Angle} \end{aligned}$$

with limits defined by

$$\begin{aligned} -180^\circ < \phi \leq 180^\circ \\ -90^\circ \leq \theta \leq 90^\circ \\ 0^\circ \leq \psi < 360^\circ \end{aligned}$$

Although Euler angles are perhaps the most intuitive way of defining orientation, for speed of computation and to avoid gimbal lock, the orientation can also be defined using quaternions. Just like Euler angles, there are multiple methods for defining a quaternion orientation. Here we use a common definition for aircraft applications [30]. For a given set of Euler angles, the corresponding four components of the quaternion representation can be computed from

$$\begin{Bmatrix} e_0 \\ e_x \\ e_y \\ e_z \end{Bmatrix} = \pm \begin{Bmatrix} C_{\phi/2}C_{\theta/2}C_{\psi/2} + S_{\phi/2}S_{\theta/2}S_{\psi/2} \\ S_{\phi/2}C_{\theta/2}C_{\psi/2} - C_{\phi/2}S_{\theta/2}S_{\psi/2} \\ C_{\phi/2}S_{\theta/2}C_{\psi/2} + S_{\phi/2}C_{\theta/2}S_{\psi/2} \\ C_{\phi/2}C_{\theta/2}S_{\psi/2} - S_{\phi/2}S_{\theta/2}C_{\psi/2} \end{Bmatrix} \tag{105}$$

Likewise, given a quaternion representation, the corresponding Euler angles can be computed from the following

algorithm:

$$
\begin{aligned}
&\text{if}(e_0 e_y - e_x e_z = 0.5) \\
&\qquad \begin{Bmatrix} \phi \\ \theta \\ \psi \end{Bmatrix} = \begin{Bmatrix} 2\sin^{-1}[e_x/\cos(\pi/4)] + \psi \\ \pi/2 \\ \text{arbitrary} \end{Bmatrix} \\
&\text{if}(e_0 e_y - e_x e_z = -0.5) \\
&\qquad \begin{Bmatrix} \phi \\ \theta \\ \psi \end{Bmatrix} = \begin{Bmatrix} 2\sin^{-1}[e_x/\cos(\pi/4)] - \psi \\ -\pi/2 \\ \text{arbitrary} \end{Bmatrix} \\
&\text{else} \\
&\qquad \begin{Bmatrix} \phi \\ \theta \\ \psi \end{Bmatrix} = \begin{Bmatrix} \text{atan2}[2(e_0 e_x + e_y e_z), (e_0^2 + e_z^2 - e_x^2 - e_y^2)] \\ \sin^{-1}[2(e_0 e_y - e_x e_z)] \\ \text{atan2}[2(e_0 e_z + e_x e_y), (e_0^2 + e_x^2 - e_y^2 - e_z^2)] \end{Bmatrix}
\end{aligned}
\tag{106}
$$

Let $[\mathbf{R}]$ be a rotation matrix such that the components of a vector in the component coordinate system can be expressed in the aircraft coordinate system using the transformation

$$
\begin{Bmatrix} v_{x_a} \\ v_{y_a} \\ v_{z_a} \end{Bmatrix} = [\mathbf{R}] \begin{Bmatrix} v_{x_c} \\ v_{y_c} \\ v_{z_c} \end{Bmatrix} \tag{107}
$$

Using the Euler angle and quaternion definitions above, the rotation matrix $[\mathbf{R}]$ can be written in Euler angles or quaternions as

$$
\begin{aligned}
[\mathbf{R}] &= \begin{bmatrix} C_\theta C_\psi & S_\phi S_\theta C_\psi - C_\phi S_\psi & C_\phi S_\theta C_\psi + S_\phi S_\psi \\ C_\theta S_\psi & S_\phi S_\theta S_\psi + C_\phi C_\psi & C_\phi S_\theta S_\psi - S_\phi C_\psi \\ -S_\theta & S_\phi C_\theta & C_\phi C_\theta \end{bmatrix} \\
&= \begin{bmatrix} e_x^2 + e_0^2 - e_y^2 - e_z^2 & 2(e_x e_y - e_z e_0) & 2(e_x e_z + e_y e_0) \\ 2(e_x e_y + e_z e_0) & e_y^2 + e_0^2 - e_x^2 - e_z^2 & 2(e_y e_z - e_x e_0) \\ 2(e_x e_z - e_y e_0) & 2(e_y e_z + e_x e_0) & e_z^2 + e_0^2 - e_x^2 - e_y^2 \end{bmatrix}
\end{aligned}
\tag{108}
$$

In general, a component can have nonzero values for all Euler angles and all quaternion components. However, for most aircraft, the rotation matrix $[\mathbf{R}]$ for the wing is a function of only the dihedral. Because dihedral is a rotation about the aircraft x axis, the Euler angles θ and ψ are both zero. Using these Euler angles in Eq. (108) gives

$$
[\mathbf{R}] = \begin{bmatrix} 1 & 0 & 0 \\ 0 & C_\phi & -S_\phi \\ 0 & S_\phi & C_\phi \end{bmatrix} \tag{109}
$$

For a right wing $\phi = -\Gamma$, and for a left wing, $\phi = \Gamma$ where a positive value for Γ represents a positive dihedral angle. From Eq. (50), a general relation for any wing dihedral can be written as

$$
\phi = -\delta\Gamma \tag{110}
$$

2. Position

The position of each component can be defined relative to the aircraft coordinate system in Cartesian coordinates. Here we will denote the position of the origin of each component relative to the origin of the aircraft coordinate system as $\mathbf{r}_o$, and the position of the CG of the each component relative to the origin of the aircraft coordinate system as $\mathbf{r}$. The

CG location of the cuboid, cylinder, sphere, and rotor relative to the aircraft origin are simple to find, since they are equivalent to the position of the origin of each of those components relative to the aircraft origin. This gives

$$\mathbf{r} = \mathbf{r}_o \tag{111}$$

The CG location of the wing relative to the aircraft origin requires some additional steps, since the CG of the wing is not coincident with the origin of the wing chosen in this development. The CG position of a wing segment relative to the aircraft coordinate system can be computed from

$$\mathbf{r} = \mathbf{r}_o + [\mathbf{R}] \begin{Bmatrix} \bar{x} \\ \bar{y} \\ \bar{z} \end{Bmatrix} \tag{112}$$

where $\mathbf{r}_o$ is the vector from the aircraft origin to the origin of the wing section and $[\mathbf{R}]$ is the rotation matrix of the component computed from Eq. (109).

C. Total Mass and Center of Gravity

The total mass of the aircraft is simply the summation of all component masses. This can be written as

$$m_{\text{aircraft}} = \sum_{i=1}^{N} m_i \tag{113}$$

where the subscript i represents the value for the i^{th} component. The location of the center of gravity of the complete system relative to the aircraft origin can be found from the expression

$$\mathbf{r}_{\text{aircraft}} = \frac{\sum_{i=1}^{N} m_i \mathbf{r}_i}{m_{\text{aircraft}}} \tag{114}$$

D. Total Inertia Tensor

The total inertia tensor of the complete system is obtained by summing the inertial influence of each component. However, in general, the CG of each component is not coincident with the aircraft CG, and the ordinates of the component coordinate system are not aligned with the aircraft coordinate system. Hence, the inertia tensor of each component must be rotated and translated before it can be summed to yield the total inertia tensor of the aircraft. This process requires the following steps:

1) Rotate the inertia tensor of each component from the component coordinate system to the aircraft coordinate system
2) Translate the inertia tensor of each component from the component CG location to the aircraft CG location
3) Sum the resulting inertia tensors to obtain the complete aircraft inertia tensor

Each step is outlined here.

1. Rotation

The inertia tensor of a component $[\mathbf{I}]$ can be expressed as an inertia tensor in the aircraft coordinate frame $[\mathbf{I}]_a$ using the expression

$$[\mathbf{I}]_a = [\mathbf{R}][\mathbf{I}][\mathbf{R}]^{\mathrm{T}} \tag{115}$$

2. Translation

Once the inertia tensor of each component has been rotated to the aircraft coordinate frame, the inertia tensor must be translated such that it represents inertia about the aircraft center of gravity. This can be accomplished using the parallel axis theorem.

Let $\mathbf{s}$ be a vector in the aircraft coordinate system that extends from the CG location of the i^{th} component $\mathbf{r}_i$ to the aircraft CG location $\mathbf{r}_{\text{aircraft}}$. This gives $\mathbf{s} = \mathbf{r}_{\text{aircraft}} - \mathbf{r}_i$. The inertia tensor of the component evaluated at the aircraft CG location can be found using the parallel axis theorem

$$[\mathbf{I}]_c = [\mathbf{I}]_a + m\left[(\mathbf{s}\cdot\mathbf{s})[\mathbf{E}] - \mathbf{s}\mathbf{s}^{\mathrm{T}}\right] \tag{116}$$

where m is the mass of the component, and $[\mathbf{E}]$ is again the $3x3$ identity matrix.

3. Summation

The total inertia of the aircraft about the aircraft CG is simply the sum of all inertia tensors, one for each component, which have been rotated and translated to be about the aircraft CG as shown in Eq. (116). This gives

$$[\mathbf{I}]_{\text{aircraft}} = \sum_{i=1}^{N} [\mathbf{I}]_{c_i} \tag{117}$$

E. Angular Momentum of Spinning Rotors

In the absence of aircraft rotation, the angular momentum of the aircraft can still be non-zero if it includes rotating rotors. The angular momentum due to rotating machinery such as propellers, jet engines, or other rotor blades will be referred to here as *gyroscopic effects*. The angular momentum of the individual rotors about the component axis of rotation can be computed from Eq. (104). A gyroscopic vector for the entire aircraft can be obtained by summing the influence of the gyroscopic effects from each individual component

$$\mathbf{h}_{\text{aircraft}} \equiv \begin{Bmatrix} h_{x_b} \\ h_{y_b} \\ h_{z_b} \end{Bmatrix} = \sum_{i=1}^{n} [\mathbf{R}]_i \mathbf{h}_i \tag{118}$$

where n is the number of rotors and $[\mathbf{R}]$ is the rotation matrix of the component computed from Eq. (108). When the gyroscopic effects are applied to the aircraft equations of motion, the components of the total gyroscopic vector $\mathbf{h}_{\text{aircraft}}$ are often written in a tensor form $[\mathbf{h}]$ as defined by [31]

$$[\mathbf{h}]_{\text{aircraft}} \equiv \begin{bmatrix} 0 & -h_{z_b} & h_{y_b} \\ h_{z_b} & 0 & -h_{x_b} \\ -h_{y_b} & h_{x_b} & 0 \end{bmatrix} \tag{119}$$

F. Additional Comments

From the development above, we see that the mass properties of the entire aircraft can be modeled by summing the influences of the individual components. Because of this, it is quite simple to use the components listed above for much more complex geometries. For example, although the wing was treated as a single object of constant density throughout, additional internal complexity of the wing can be modeled by adding and subtracting other simple shapes. Empty regions between spars and ribs can be modeled by adding cuboids within the wing with negative density values of the same magnitude as the wing density. A fuel tank can be modeled by adding a cuboid with density in addition to the wing density. In general, internal hollow regions can be added within any external solid region by simply setting the density of the internal region equal to the negative of the external object density. This method can be used to create cavities in which other structures can be added, such as actuators, internal engine turbine blades, payloads, hydraulic systems, etc. Hence, the simple shapes included here can be used to represent much more complex internal structures and mass distributions than may first appear obvious.

VI. Validation Studies

The forgoing analysis should be exact for any component that exactly matches the component geometries described. To evaluate the accuracy that might be expected when using the wing segment component to represent a realistic wing geometry, several validation cases were performed. These cases were also used to ensure that the mathematical development given above is correct.

A. Validity Study : A Simple Foam Wing

The first study is used to examine the accuracy of the present method in determining the mass and inertia properties of a simple constant-density wing. We begin with a rectangular wing having a symmetric airfoil. This wing will be called the base case. Perturbations in the following properties are then be examined: linear taper (taper), linear thickness (thickness), constant camber (camber), airfoil thickness distribution (Clark Y and diamond), sweep, and a combination

of all of the perturbations (all). To reflect the combination of all perturbations, airfoils were chosen from the same family as those used in the 'airfoil' wing, but with thickness and camber properties providing linear changes in each characteristic. Table 2 shows the properties for each of the perturbation studies performed. For the diamond airfoil, the parameters $\tau_m = 12\%$, and $\hat{x}_m = 0.5$ were used.

Table 2 Wing Properties

wing name	side	b [ft]	c_r [ft]	c_t [ft]	root airfoil	tip airfoil	Λ [deg]
rectangular	right	8	1	1	NACA 0012	NACA 0012	0
taper	right	8	1.5	0.5	NACA 0012	NACA 0012	0
thickness	right	8	1	1	NACA 0016	NACA 0008	0
camber	right	8	1	1	NACA 4812	NACA 4812	0
Clark Y	right	8	1	1	Clark Y	Clark Y	0
diamond	right	8	1	1	Diamond Airfoil	Diamond Airfoil	0
sweep	right	8	1	1	NACA 0012	NACA 0012	14
all properties	right	8	1.5	0.5	NACA 4816	NACA 4808	14

A wing was created for each of these cases in the CAD package Solid Works^{TM}. Each wing was given a density of 0.25 slugs/ft^3. The mass and inertial properties for the CAD wings and those determined using the present method are given in Tables D.1 - D.4. Note that the results were truncated to four digits following the decimal point. The percent difference between the mass and inertial results given in those tables are given in Tables 3 and 4, respectively.

Table 3 Percent difference between analyses of mass properties in simple wing study.

name	m	$\bar{x}$	$\bar{y}$	$\bar{z}$
rectangular	0.00 %	0.00 %	0.00 %	0.00 %
taper	0.00 %	-0.05 %	0.00 %	0.00 %
thickness	-0.12 %	0.29 %	-0.02 %	0.00 %
camber	0.30 %	0.12 %	0.00 %	100.00 %
Clark Y	0.00 %	-0.35 %	0.00 %	100.00 %
diamond	0.00 %	0.00 %	0.00 %	0.00 %
sweep	0.00 %	0.00 %	0.00 %	0.00 %
all	1.65 %	0.27 %	0.64 %	100.00 %

Table 4 Percent difference between analyses of inertial properties in simple wing study.

name	I_{xx_c}	I_{yy_c}	I_{zz_c}	I_{xy_c}	I_{xz_c}	I_{yz_c}
rectangular	0.01 %	0.00 %	0.00 %	0.00 %	0.00 %	0.00 %
taper	0.01 %	0.00 %	0.00 %	0.00 %	0.00 %	0.00 %
thickness	-0.08 %	0.00 %	-0.08 %	0.00 %	0.00 %	0.00 %
camber	0.27 %	1.08 %	0.27 %	0.00 %	100.00 %	0.00 %
Clark Y	0.00 %	0.00 %	-0.01 %	0.00 %	0.00 %	0.00 %
diamond	0.00 %	0.00 %	0.00 %	0.00 %	0.00 %	0.00 %
sweep	0.01 %	0.00 %	0.00 %	0.00 %	0.00 %	0.00 %
all	1.89 %	1.83 %	1.88 %	1.69 %	0.00 %	100.00 %

Results in these tables show that the method presented above is accurate to within less than 2% for all mass properties

considered, except for $\bar{z}$ and I_{yz_c}. The error seen in these two terms is due to the fact that camber has been neglected in the analysis, whereas the "camber" and "all" wings included nonzero camber. While the error in these two terms appears large in percentage form, D.1 - D.4 show that the dimensional values of these parameters are generally two orders of magnitude smaller than their dimensional counterparts. For example, $\bar{z} = -.0323$ whereas $\bar{x} = -0.8178$. Hence, although the percent error is large, the actual error in these terms is small. The very small error $< 1\%$ in many of the other terms is likely due to a difference in how linear taper and thickness distributions are handled in the method presented here compared to the splines used by Solid Works^{TM}. In general, the results presented here show that the method presented above is extremely accurate for individual wing sections with geometric properties in the ranges of parameters commonly used on aircraft.

B. Assumption Study : Common Research Model

The Common Research Model (CRM) * developed by NASA is a convenient airframe for the purposes of this study. A CAD model of this airframe is shown in Fig. 11. We will examine the buildup of error across the last three assumptions utilized in the development of this method: namely, neglecting camber and assuming a NACA 4-digit thickness distribution, neglecting twist, and linear and constant properties (causing a straight quarter-chord line). The geometry used for the CRM models is taken from the discretized model determined by Taylor and Hunsaker [32]. The constant section properties derived from this model and used in the following analyses are given in Table D.5. The airfoil max thickness values were determined from the airfoil data set† published by Taylor and Hunsaker using an airfoil analysis tool called AirfoilDatabase‡. The calculated mass properties for the following analyses are given in Tables D.6 and D.7.

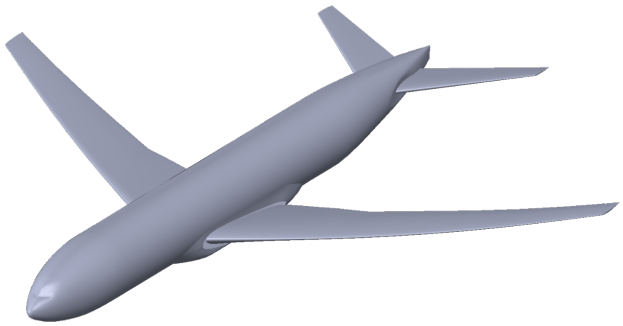

Fig. 11 CAD model of the CRM.

To study the accuracy of the wing segment approximation developed in this paper, the fuselage was not included in the following analysis. The first mass study was performed on a CAD model of constant density of the outer mold line (OML) of the aircraft. The density for this model was determined assuming a mass of 220,240 kg (15091.2336 slugs) [32]. This is the figure on the far left in Fig. 12. This CAD model has a traditional airfoil section-shape, linear taper, linear airfoil changes, linear twist, linear dihedral, and linear sweep.

The second mass study was performed on a CAD model of constant density of the outer mold line (OML) of the aircraft with the airfoil having a symmetric thickness distribution. The density for this model was determined assuming an equivalent mass to the CRM OML model. This is the second figure from the left in Fig. 12. This CAD model has linear taper, linear airfoil changes, linear twist, linear dihedral, and linear sweep.

The third mass study was performed on a CAD model of constant density of the outer mold line (OML) of the aircraft with the airfoil having a symmetric thickness distribution, and neglecting twist. The density for this model was determined assuming an equivalent mass to the CRM OML model. This is the third figure from the left in Fig. 12. This CAD model has linear taper, linear airfoil changes, linear dihedral, and linear sweep.

The fourth mass study was performed on a CAD model of constant density of the aircraft with the distinct sections having straight quarter-chord lines. The density for this model was determined assuming an equivalent mass to the CRM CAD model. This is the far right figure in Fig. 12. As this model has linear taper, linear airfoil changes (via linear

*commonresearchmodel.larc.nasa.gov

†https://digitalcommons.usu.edu/all_datasets/125 (doi: 10.26078/8nv8-yj03)

‡https://github.com/usuaero/AirfoilDatabase

changes in thickness and camber), constant dihedral and sweep, the taper and angles were calculated so the quarter-chord of the root and tip of each segment would align which the corresponding positions on the actual model.

Fig. 12 Validation CAD models of the CRM.

Below in Tables 5 - 10 are the percent differences between the analysis in each column with respect to that in each row. Each of the above mass studies are compared with each other and with the equations developed in the presented method.

Table 5 Percent difference between analyses of x_{cg} of the CRM.

Analysis	uncambered	no twist	straight quarter-chord	present method
OML	0.78 %	0.70 %	0.70 %	0.70 %
uncambered		-0.08 %	-0.09 %	-0.09 %
no twist			-0.01 %	-0.01 %
straight quarter-chord				0.00 %

Table 6 Percent difference between analyses of z_{cg} of the CRM.

Analysis	uncambered	no twist	straight quarter-chord	present method
OML	-18.95 %	-44.98 %	-46.30 %	-46.29 %
uncambered		-21.88 %	-22.99 %	-22.98 %
no twist			-0.91 %	-0.90 %
straight quarter-chord				0.01 %

Table 7 Percent difference between analyses of I_{xx_b} of the CRM.

Analysis	uncambered	no twist	straight quarter-chord	present method
OML	0.77 %	0.81 %	0.80 %	0.81 %
uncambered		0.04 %	0.03 %	0.03 %
no twist			-0.01 %	0.00 %
straight quarter-chord				0.01 %

Table 8 Percent difference between analyses of I_{yy_b} of the CRM.

Analysis	uncambered	no twist	straight quarter-chord	present method
OML	0.77 %	0.83 %	0.85 %	0.86 %
uncambered		0.06 %	0.08 %	0.09 %
no twist			0.02 %	0.03 %
straight quarter-chord				0.01 %

Table 9 Percent difference between analyses of I_{zz_b} of the CRM.

Analysis	uncambered	no twist	straight quarter-chord	present method
OML	0.54 %	0.42 %	0.42 %	0.43 %
uncambered		-0.12 %	-0.12 %	-0.11 %
no twist			0.00 %	0.01 %
straight quarter-chord				0.01 %

Table 10 Percent difference between analyses of I_{xz_b} of the CRM.

Analysis	uncambered	no twist	straight quarter-chord	present method
OML	8.04 %	9.69 %	10.03 %	10.04 %
uncambered		1.79 %	2.16 %	2.17 %
no twist			0.38 %	0.39 %
straight quarter-chord				0.01 %

The x centroid location is within 1% compared to the constant density OML model. The error in the z direction is much greater. This is due to the values for the z_{cg} location being typically 1-2 orders of magnitude smaller than those for x_{cg}.

The moments of inertia percent differences of the presented method are less than 1% compared to that of the constant density OML model. The larger differences in the products of inertia percent differences is due to slight asymmetry in the CAD OML model which are not extant in the presented method. This study demonstrates that camber, twist, and nonlinear sweep and dihedral have only minimal affect on the wing inertial properties of the CRM. We note that neglecting camber generally is responsible for the largest error in the simplified model of the CRM. Error due to neglecting twist and assuming linear and constant properties across the wing segments generally have an order of magnitude smaller effect on the accuracy of the presented method for the CRM.

C. Constant Density Assumption Study : Horizon

Horizon is a 3D-printed flying-wing aircraft designed, built, and flown by the USU AeroLab. A CAD model of Horizon is shown in Fig. 13[§]. The aircraft has a complex inner geometry due to the spar structure and control-surface morphing geometry. Due to varying requirements, several components of the aircraft assembly have different densities. The constant section properties derived from this model and used in the following analyses are given in Table D.8. The calculated mass properties for the following analyses are given in Tables D.9 and D.10.

[§] thingiverse.com/thing:4672874

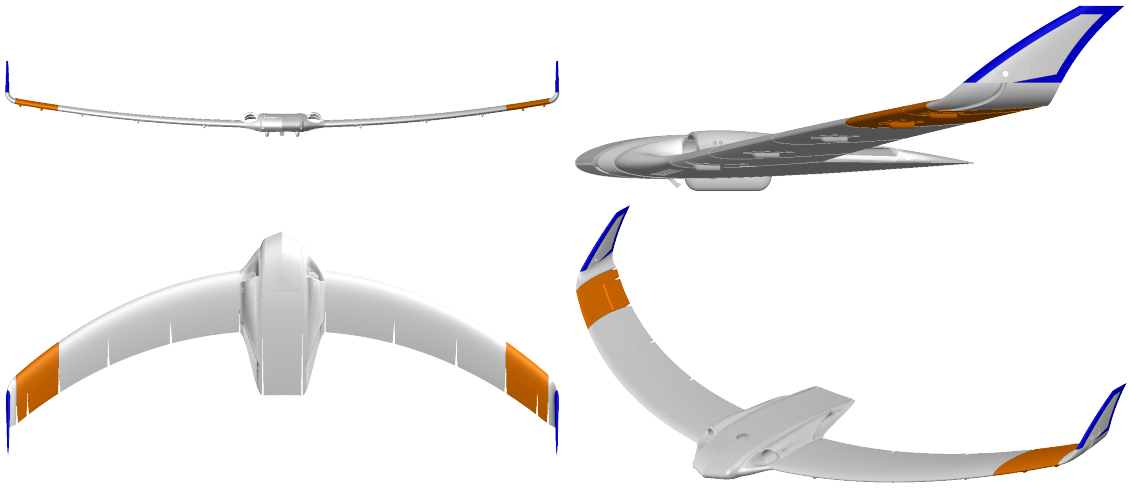

Fig. 13 CAD model of the Horizon aircraft.

The densities of each segment were determined from the physical prints. While the density of Polylactic Acid (PLA) is 2.406 slugs/ft^3, 3D-printed parts tend to be more porous than a solid model. The slicer-projected and actual mass of several parts were averaged, giving a 93.53% (6.47% decrease) mass during printing, and (assuming no change in volume) a 95.53% PLA density. The PLA density used was calculated to be the decreased percentage of PLA density, 2.25 slugs/ft^3. The densities of various components were calculated off their respective infill percentage during printing, namely 100% (2.25 slugs/ft^3), 50% (1.125 slugs/ft^3), 30% (0.675 slugs/ft^3), 20% (0.45 slugs/ft^3), and 6% (0.135 slugs/ft^3). These various densities were applied to their respective part in the CAD model. The Solid Works^{TM} mass analysis tool was then used to determine the mass, cg-location, and inertia tensor of the aircraft.

We will now discuss the five mass studies performed on this aircraft. The first four are performed using Solid Works^{TM} to demonstrate the effect of the various assumptions used in the development of the presented method. Each of these CAD models is shown in Fig. 14. The fifth mass study is performed using the presented method.

The first mass study was performed on the actual Horizon CAD model. This is the far left figure in Fig. 14. Segments of higher density are rendered in a darker color, and those of lower densities in a lighter color. This CAD model has variable density, a traditional airfoil section-shape, and linearly tapered sections, linear dihedral, and linear sweep.

The second mass study was performed on a CAD model of constant density of the outer mold line (OML) of the aircraft. The density for this model was determined assuming an equivalent mass to the Horizon CAD model. This is the second figure from the left in Fig. 14. This CAD model has a traditional airfoil section-shape, and linearly tapered sections, linear dihedral, and linear sweep.

The third mass study was performed on a CAD model of constant density of the outer mold line (OML) of the aircraft with the airfoil replaced by an uncambered airfoil using the NACA 4-digit thickness distribution of similar chord-length and thickness. The density for this model was determined assuming an equivalent mass to the Horizon CAD model. This is the third figure from the left in Fig. 14. This CAD model has linearly tapered sections, linear dihedral, and linear sweep.

The fourth mass study was performed on a CAD model of constant density of the aircraft with the distinct sections having straight quarter-chord lines. The density for this model was determined assuming an equivalent mass to the Horizon CAD model. This is the far right figure in Fig. 14. As this model has linearly tapered sections, constant dihedral and sweep, the geometric angles were calculated so the quarter-chord of the root and tip of each segment would align which the corresponding positions on the actual model.

Fig. 14 Validation CAD models of the Horizon aircraft.

Below in Tables 11 - 16 are the percent differences between the analysis in each column with respect to that in each row. Each of the above mass studies are compared with each other and with the equations developed in the presented method. Results which are between two zero values or are uninformative are not presented. These include the tables for m, I_{xy_b}, and I_{yz_b} as the percent differences were all zeros.

Table 11 Percent difference between analyses of x_{cg} of Horizon.

Analysis	OML	uncambered	straight quarter-chord	present method
actual	11.22 %	11.07 %	9.51 %	9.51 %
OML		-0.17 %	-1.92 %	-1.92 %
uncambered			-1.75 %	-1.75 %
straight quarter-chord				0.00 %

Table 12 Percent difference between analyses of z_{cg} of Horizon.

Analysis	OML	uncambered	straight quarter-chord	present method
actual	8.33 %	27.75 %	26.16 %	26.16 %
OML		21.19 %	19.45 %	19.45 %
uncambered			-2.21 %	-2.21 %
straight quarter-chord				0.00 %

Table 13 Percent difference between analyses of I_{xx_b} of Horizon.

Analysis	OML	uncambered	straight quarter-chord	present method
actual	19.50 %	19.19 %	19.40 %	19.40 %
OML		-0.39 %	-0.13 %	-0.13 %
uncambered			0.27 %	0.27 %
straight quarter-chord				0.00 %

Table 14 Percent difference between analyses of I_{yy_b} of Horizon.

Analysis	OML	uncambered	straight quarter-chord	present method
actual	-3.73 %	-4.43 %	-4.96 %	-4.96 %
OML		-0.67 %	-1.18 %	-1.18 %
uncambered			-0.50 %	-0.50 %
straight quarter-chord				0.00 %

Table 15 Percent difference between analyses of I_{zz_b} of Horizon.

Analysis	OML	uncambered	straight quarter-chord	present method
actual	18.04 %	17.77 %	17.95 %	17.95 %
OML		-0.33 %	-0.12 %	-0.12 %
uncambered			0.21 %	0.21 %
straight quarter-chord				0.00 %

Table 16 Percent difference between analyses of I_{xz_b} of Horizon.

Analysis	OML	uncambered	straight quarter-chord	present method
actual	-7.03 %	-12.11 %	-13.67 %	-13.67 %
OML		-4.74 %	-6.20 %	-6.20 %
uncambered			-1.39 %	-1.39 %
straight quarter-chord				0.00 %

The center of gravity location is affected less by the constant density assumption than the moments of inertia. As with the CRM study, the decreasing accuracy with each new assumption is nearly an order of magnitude smaller for this case study of the Horizon aircraft. Most importantly, the constant density assumption affects the accuracy of the presented method, generally on the order of 20%. In other words, computing the inertial properties of a typical wing with complex internal structure by assuming a constant density within the wing can cause errors in the estimation of about 20%. Better results can be obtained by not assuming the wing has constant density throughout. For example, the method presented in this paper can be used to estimate complex structures within a wing by adding objects of varying density (including some negative to represent hollow regions) within the wing.

Though this density assumption error is significant, we also recommend this analysis for preliminary design of full sized aircraft. This roughly 20% error in the absence of knowing the internal structure can give the designer a scope of what the final design mass and inertial properties will be, based on these preliminary estimates.

As seen in the various analyses, the accuracy of the presented method is best for constant or near-constant-density wings which have constant sweep or dihedral. Most linearly-changing characteristics tend to decrease the accuracy of the method. Further research could examine a shelled airfoil-section with wingbox model using the presented method of inertial derivation. Further research could also examine the effect of airfoil maximum camber on mass and inertial characteristics.

VII. Conclusion

Typical methods for determining the mass and inertial characteristics of on aircraft can be difficult and complex. Frequently, CAD methods are used to determine the inertia of aircraft in preliminary design stages. However, using CAD requires intricate modeling of the internal and external geometry of the aircraft, and is time consuming for initial design phases. A simple method was presented here for estimating the mass and inertial properties of complete aircraft. This method consists of closed-form solutions for a number of simple geometries, assuming each geometry has constant density. For a wing and rotor, the effects of twist, pitch, and airfoil camber were neglected.

The various coordinate frames and geometric properties of each component type were defined and visualized for the benefit of the reader. The closed form equations for the mass, center of gravity, and inertia tensor components were then derived and presented for each component. The derivation and closed form equations for the total mass, center of gravity, and inertia tensor of a wing segment and rotor were also presented. A change of variables in the chordwise, spanwise, and normal directions of a wing segment were developed and applied in order to produce simplified closed-form solutions for these otherwise complex geometries. These closed-form solutions can be used to account for arbitrary airfoil thickness distributions. The process of computing the mass and inertial properties of each component, as well as summing these to compute the total mass and inertia of the complete aircraft is explained in detail.

Several validation cases were included to demonstrate the utility and accuracy of the method. The full-aircraft studies demonstrated that making the assumption of a wing with constant density instead of modeling the complex

internal structure of the wing can result in inertial prediction errors on the order of 20%. Other approximations including neglecting camber, or assuming constant sweep and dihedral generally introduce errors on the order of 1–2% in the moments of inertia. This method is recommended for use in the preliminary design phase of aircraft development. Complete aircraft can be accurately modeled by including components of both positive and negative densities to represent complex internal structures and components. A quick and simple method, this can be used to determine an initial estimate for the inertia and mass distributions of an aircraft. Further work could examine adding twist, linear dihedral, linear sweep, and improving the accuracy of the method for wings with extreme density variability.

A. Wing-Segment Integrals

A. Integration Components

The required volume, moment, and inertia derivations can be shown to be varying sums of volume integrals of terms of the form $x^i y^j z^k$ where i, j, and k are each positive integers. For simplification these integrals ($S_{i,j,k}$) will be shown here and used in the body of the present paper. These integrals will depend on the following functions

$$\begin{aligned} c(\hat{y}) &= (c_t - c_r)\,\hat{y} + c_r \\ \tau_m(\hat{y}) &= (\tau_t - \tau_r)\,\hat{y} + \tau_r \\ \tau(\hat{x}, \hat{y}) &= \tau_m(\hat{y})\mu(\hat{x}) \end{aligned}$$

The integrations shown will follow the formula

$$S_{i,j,k} = \int_0^b \int_{-\frac{3}{4}c(y)}^{\frac{1}{4}c(y)} \int_{-\frac{1}{2}\tau_m(y)\mu(x)c(y)}^{\frac{1}{2}\tau_m(y)\mu(x)c(y)} x^i y^j z^k \, dz \, dx \, dy \tag{A.1}$$

We can insert the change of variables and corresponding derivatives

$$x = c(\hat{y})\left(\frac{1}{4} - \hat{x}\right) \qquad dx = -c(\hat{y})d\hat{x} \tag{A.2}$$

$$y = b\hat{y} \qquad dy = bd\hat{y} \tag{A.3}$$

$$z = \tau_m(\hat{y})\mu(\hat{x})c(\hat{y})\left(\frac{1}{2} - \hat{z}\right) \qquad dz = -\tau_m(\hat{y})\mu(\hat{x})c(\hat{y})d\hat{z} \tag{A.4}$$

resulting in the integral

$$S_{i,j,k} = \int_0^1 \int_0^1 \int_0^1 c(\hat{y})^i \left(\frac{1}{4} - \hat{x}\right)^i (b\hat{y})^j \, \tau_m(\hat{y})^k \mu(\hat{x})^k c(\hat{y})^k \left(\frac{1}{2} - \hat{z}\right)^k \, \tau_m(\hat{y})\mu(\hat{x})c(\hat{y})d\hat{z}\, c(\hat{y})d\hat{x}\, bd\hat{y} \tag{A.5}$$

which is simplified to

$$S_{i,j,k} = b^{j+1} \int_0^1 \tau_m(\hat{y})^{k+1} c(\hat{y})^{i+k+2} \hat{y}^j \int_0^1 \mu(\hat{x})^{k+1} \left(\frac{1}{4} - \hat{x}\right)^i \int_0^1 \left(\frac{1}{2} - \hat{z}\right)^k \, d\hat{z}\, d\hat{x}\, d\hat{y} \tag{A.6}$$

The thickness distribution $\mu(\hat{x})$ can be removed from this integral (note, all other components of this integration are independent of the thickness distribution) and determined separately for an arbitrary thickness distribution. These various integrals will be termed as υ values here, and defined in Appendix C. The final integral equation that will be used is

$$S_{i,j,k} = \left(\frac{\int_0^1 \mu(\hat{x})^{k+1} \left(\frac{1}{4} - \hat{x}\right)^i d\hat{x}}{\int_0^1 \left(\frac{1}{4} - \hat{x}\right)^i d\hat{x}} \right) b^{j+1} \int_0^1 \tau_m(\hat{y})^{k+1} c(\hat{y})^{i+k+2} \hat{y}^j \int_0^1 \left(\frac{1}{4} - \hat{x}\right)^i \int_0^1 \left(\frac{1}{2} - \hat{z}\right)^k \, d\hat{z}\, d\hat{x}\, d\hat{y} \tag{A.7}$$

The all-zero-term case can be determined as

$$\begin{aligned} S_{0,0,0} &= \upsilon_0 b \int_0^1 \tau_m(\hat{y}) c(\hat{y})^2 \int_0^1 \int_0^1 d\hat{z}\, d\hat{x}\, d\hat{y} \\ &= \upsilon_0 \frac{b}{12} \left[\tau_r \left(3c_r^2 + 2c_r c_t + c_t^2 \right) + \tau_t \left(c_r^2 + 2c_r c_t + 3c_t^2 \right) \right] \end{aligned} \tag{A.8}$$

The single-term cases can be determined as

$$S_{1,0,0} = \upsilon_1 b \int_0^1 \tau_m(\hat{y}) c(\hat{y})^3 \int_0^1 \left(\frac{1}{4} - \hat{x}\right) \int_0^1 d\hat{z}\, d\hat{x}\, d\hat{y}$$
$$= -\upsilon_1 \frac{b}{80} \left[\tau_r \left(4c_r^3 + 3c_r^2 c_t + 2c_r c_t^2 + c_t^3\right) + \tau_t \left(c_r^3 + 2c_r^2 c_t + 3c_r c_t^2 + 4c_t^3\right)\right] \tag{A.9}$$

$$S_{0,1,0} = \upsilon_0 b^2 \int_0^1 \tau_m(\hat{y}) c(\hat{y})^2 \hat{y} \int_0^1 \int_0^1 d\hat{z}\, d\hat{x}\, d\hat{y}$$
$$= \upsilon_0 \frac{b^2}{60} \left[\tau_r \left(3c_r^2 + 4c_r c_t + 3c_t^2\right) + 2\tau_t \left(c_r^2 + 3c_r c_t + 6c_t^2\right)\right] \tag{A.10}$$

$$S_{0,0,1} = \upsilon_m b \int_0^1 \tau_m(\hat{y})^2 c(\hat{y})^3 \int_0^1 \int_0^1 \left(\frac{1}{2} - \hat{z}\right) d\hat{z}\, d\hat{x}\, d\hat{y} = 0 \tag{A.11}$$

The double-term cases can be split into two categories: combinations of single terms and single squared terms. The combination of single terms cases can be determined as

$$S_{1,1,0} = \upsilon_1 b^2 \int_0^1 \tau_m(\hat{y}) c(\hat{y})^3 \hat{y} \int_0^1 \left(\frac{1}{4} - \hat{x}\right) \int_0^1 d\hat{z}\, d\hat{x}\, d\hat{y}$$
$$= -\upsilon_1 \frac{b^2}{240} \left[\tau_r \left(c_r + c_t\right) \left(2c_r^2 + c_r c_t + 2c_t^2\right) + \tau_t \left(c_r^3 + 3c_r^2 c_t + 6c_r c_t^2 + 10c_t^3\right)\right] \tag{A.12}$$

$$S_{1,0,1} = \upsilon_n b \int_0^1 \tau_m(\hat{y})^2 c(\hat{y})^4 \int_0^1 \left(\frac{1}{4} - \hat{x}\right) \int_0^1 \left(\frac{1}{2} - \hat{z}\right) d\hat{z}\, d\hat{x}\, d\hat{y} = 0 \tag{A.13}$$

$$S_{0,1,1} = \upsilon_o b^2 \int_0^1 \tau_m(\hat{y})^2 c(\hat{y})^3 \hat{y} \int_0^1 \int_0^1 \left(\frac{1}{2} - \hat{z}\right) d\hat{z}\, d\hat{x}\, d\hat{y} = 0 \tag{A.14}$$

The single squared-term cases can be determined as

$$S_{2,0,0} = \upsilon_2 b \int_0^1 \tau_m(\hat{y}) c(\hat{y})^4 \int_0^1 \left(\frac{1}{4} - \hat{x}\right)^2 \int_0^1 d\hat{z}\, d\hat{x}\, d\hat{y}$$
$$= \upsilon_2 \frac{7b}{1440} \left[\tau_r \left(5c_r^4 + 4c_r^3 c_t + 3c_r^2 c_t^2 + 2c_r c_t^3 + c_t^4\right) + \tau_t \left(c_r^4 + 2c_r^3 c_t + 3c_r^2 c_t^2 + 4c_r c_t^3 + 5c_t^4\right)\right] \tag{A.15}$$

$$S_{0,2,0} = \upsilon_0 b^3 \int_0^1 \tau_m(\hat{y}) c(\hat{y})^2 \hat{y}^2 \int_0^1 \int_0^1 d\hat{z}\, d\hat{x}\, d\hat{y}$$
$$= \upsilon_0 \frac{b^3}{60} \left[\tau_r \left(c_r^2 + 2c_r c_t + 2c_t^2\right) + \tau_t \left(c_r^2 + 4c_r c_t + 10c_t^2\right)\right] \tag{A.16}$$

$$S_{0,0,2} = \upsilon_3 b \int_0^1 \tau_m(\hat{y})^3 c(\hat{y})^4 \int_0^1 \int_0^1 \left(\frac{1}{2} - \hat{z}\right)^2 d\hat{z}\, d\hat{x}\, d\hat{y}$$
$$= \upsilon_3 \frac{b}{3360} \Big[\tau_r^3 \left(35c_r^4 + 20c_r^3 c_t + 10c_r^2 c_t^2 + 4c_r c_t^3 + c_t^4\right) + \tau_r^2 \tau_t \left(15c_r^4 + 20c_r^3 c_t + 18c_r^2 c_t^2 + 12c_r c_t^3 + 5c_t^4\right)$$
$$+ \tau_r \tau_t^2 \left(5c_r^4 + 12c_r^3 c_t + 18c_r^2 c_t^2 + 20c_r c_t^3 + 15c_t^4\right) + \tau_t^3 \left(c_r^4 + 4c_r^3 c_t + 10c_r^2 c_t^2 + 20c_r c_t^3 + 35c_t^4\right)\Big] \tag{A.17}$$

In summary, these integrals can be written as

$$S_{0,0,0} = \frac{b}{12}\kappa_a \upsilon_0 \tag{A.18}$$

$$S_{1,0,0} = -\frac{b}{80}\kappa_b \upsilon_1 \tag{A.19}$$

$$S_{0,1,0} = \frac{b^2}{60}\kappa_c \upsilon_0 \tag{A.20}$$

$$S_{0,0,1} = S_{1,0,1} = S_{0,1,1} = 0 \tag{A.21}$$

$$S_{1,1,0} = -\frac{b^2}{240}\kappa_d \upsilon_1 \tag{A.22}$$

$$S_{2,0,0} = \frac{7b}{1440}\kappa_e \upsilon_2 \tag{A.23}$$

$$S_{0,2,0} = \frac{b^3}{60}\kappa_f \upsilon_0 \tag{A.24}$$

$$S_{0,0,2} = \frac{b}{3360}\kappa_g \upsilon_3 \tag{A.25}$$

where

$$\kappa_a \equiv \tau_r \left(3c_r^2 + 2c_r c_t + c_t^2\right) + \tau_t \left(c_r^2 + 2c_r c_t + 3c_t^2\right)$$

$$\kappa_b \equiv \tau_r \left(4c_r^3 + 3c_r^2 c_t + 2c_r c_t^2 + c_t^3\right) + \tau_t \left(c_r^3 + 2c_r^2 c_t + 3c_r c_t^2 + 4c_t^3\right)$$

$$\kappa_c \equiv \tau_r \left(3c_r^2 + 4c_r c_t + 3c_t^2\right) + 2\tau_t \left(c_r^2 + 3c_r c_t + 6c_t^2\right)$$

$$\kappa_d \equiv \tau_r \left(c_r + c_t\right)\left(2c_r^2 + c_r c_t + 2c_t^2\right) + \tau_t \left(c_r^3 + 3c_r^2 c_t + 6c_r c_t^2 + 10c_t^3\right)$$

$$\kappa_e \equiv \tau_r \left(5c_r^4 + 4c_r^3 c_t + 3c_r^2 c_t^2 + 2c_r c_t^3 + c_t^4\right) + \tau_t \left(c_r^4 + 2c_r^3 c_t + 3c_r^2 c_t^2 + 4c_r c_t^3 + 5c_t^4\right)$$

$$\kappa_f \equiv \tau_r \left(c_r^2 + 2c_r c_t + 2c_t^2\right) + \tau_t \left(c_r^2 + 4c_r c_t + 10c_t^2\right)$$

$$\kappa_g \equiv \tau_r^3 \left(35c_r^4 + 20c_r^3 c_t + 10c_r^2 c_t^2 + 4c_r c_t^3 + c_t^4\right) + \tau_r^2 \tau_t \left(15c_r^4 + 20c_r^3 c_t + 18c_r^2 c_t^2 + 12c_r c_t^3 + 5c_t^4\right)$$
$$+ \tau_r \tau_t^2 \left(5c_r^4 + 12c_r^3 c_t + 18c_r^2 c_t^2 + 20c_r c_t^3 + 15c_t^4\right) + \tau_t^3 \left(c_r^4 + 4c_r^3 c_t + 10c_r^2 c_t^2 + 20c_r c_t^3 + 35c_t^4\right)$$

and the υ coefficients are calculated in Appendix C.

B. Rotor Integrals

A. Integration Components

The required volume, moment, and inertia derivations can be shown to be varying sums of volume integrals of terms of the form $x^i y^j z^k$ where i, j, and k are each positive integers. For simplification these integrals ($T_{i,j,k}$) will be shown here and used in the body of the present paper. These integrals will depend on the following functions

$$c(r) = (c_t - c_r)\frac{(r - r_r)}{(r_t - r_r)} + c_r$$

$$\tau_m(r) = (\tau_t - \tau_r)\frac{(r - r_r)}{(r_t - r_r)} + \tau_r$$

$$h(r) = \frac{N_b \tau_m(r) c(r)^2 \upsilon_0}{2\pi r}$$

We can convert our system to a form of polar coordinates (to align the axis as we have defined for the rotor) where

$$x = x \tag{B.1}$$
$$y = r\cos\varphi \tag{B.2}$$
$$z = r\sin\varphi \tag{B.3}$$

The angle φ is the angle about the x-axis, with a counter clockwise angle being positive. As we have changed the coordinate system, we will define the inertia in this new polar coordinate frame to be

$$T_{i,j,k} = \iiint_V x^i \left(r\cos\varphi\right)^j \left(r\sin\varphi\right)^k r\,dx\,dr\,d\varphi \tag{B.4}$$

to which we can apply our bounds

$$0 \le \varphi \le 2\pi \tag{B.5}$$
$$r_r \le r \le r_t \tag{B.6}$$
$$-\frac{h(r)}{2} \le x \le \frac{h(r)}{2} \tag{B.7}$$

as

$$T_{i,j,k} = \int_0^{2\pi} \cos^j\varphi \sin^k\varphi \int_{r_r}^{r_t} r^{j+k+1} \int_{-\frac{1}{2}h(r)}^{\frac{1}{2}h(r)} x^i\,dx\,dr\,d\varphi \tag{B.8}$$

The all-zero-term case can be determined as

$$\begin{aligned} T_{0,0,0} &= \int_0^{2\pi} \int_{r_r}^{r_t} r \int_{-\frac{1}{2}h(r)}^{\frac{1}{2}h(r)} dx\,dr\,d\varphi \\ &= \frac{1}{12} N_b \kappa_a \upsilon_0 \left(r_t - r_r\right) \end{aligned} \tag{B.9}$$

The single-term cases can be determined as

$$T_{1,0,0} = \int_0^{2\pi} \int_{r_r}^{r_t} r \int_{-\frac{1}{2}h(r)}^{\frac{1}{2}h(r)} x\,dx\,dr\,d\varphi = 0 \tag{B.10}$$

$$T_{0,1,0} = \int_0^{2\pi} \cos\varphi \int_{r_r}^{r_t} r^2 \int_{-\frac{1}{2}h(r)}^{\frac{1}{2}h(r)} dx\,dr\,d\varphi = 0 \tag{B.11}$$

$$T_{0,0,1} = \int_0^{2\pi} \sin\varphi \int_{r_r}^{r_t} r^2 \int_{-\frac{1}{2}h(r)}^{\frac{1}{2}h(r)} dx\,dr\,d\varphi = 0 \tag{B.12}$$

The double-term cases can be split into two categories: combinations of single terms and single squared terms. The combination of single terms cases can be determined as

$$T_{1,1,0} = \int_0^{2\pi} \cos\varphi \int_{r_r}^{r_t} r^2 \int_{-\frac{1}{2}h(r)}^{\frac{1}{2}h(r)} x\,dx\,dr\,d\varphi = 0 \tag{B.13}$$

$$T_{1,0,1} = \int_0^{2\pi} \sin\varphi \int_{r_r}^{r_t} r^2 \int_{-\frac{1}{2}h(r)}^{\frac{1}{2}h(r)} x\,dx\,dr\,d\varphi = 0 \tag{B.14}$$

$$T_{0,1,1} = \frac{1}{2} \int_0^{2\pi} \sin(2\varphi) \int_{r_r}^{r_t} r^3 \int_{-\frac{1}{2}h(r)}^{\frac{1}{2}h(r)} dx\,dr\,d\varphi = 0 \tag{B.15}$$

The single squared-term cases can be determined as

$$T_{2,0,0} = \int_0^{2\pi} \int_{r_r}^{r_t} r \int_{-\frac{1}{2}h(r)}^{\frac{1}{2}h(r)} x^2 dx dr d\varphi$$
$$= N_b^3 v_0^3 \frac{\gamma_a r_r^{10} + \gamma_b r_r^9 r_t + \gamma_c r_r^8 r_t^2 + \gamma_d r_r^7 r_t^3 + \gamma_e r_r^6 r_t^4 + \gamma_f r_r^5 r_t^5 + \gamma_g r_r^4 r_t^6 + \gamma_h r_r^3 r_t^7 + \gamma_i r_r^2 r_t^8 + \gamma_j r_r r_t^9 + \gamma_k r_t^{10}}{13440\pi^2 r_r r_t (r_r - r_t)^9} \tag{B.16}$$

where

$$\gamma_a = -280 c_t^6 \tau_t^3 \tag{B.17}$$

$$\begin{aligned}\gamma_b = -\Big[& c_r^6(35\tau_r^3 + 15\tau_r^2\tau_t + 5\tau_r\tau_t^2 + \tau_t^3) + 6c_r^5 c_t(5\tau_r^3 + 5\tau_r^2\tau_t + 3\tau_r\tau_t^2 + \tau_t^3) \\ & + 5c_r^4 c_t^2(5\tau_r^3 + 9\tau_r^2\tau_t + 9\tau_r\tau_t^2 + 5\tau_t^3) + 20c_r^3 c_t^3(\tau_r^3 + 3\tau_r^2\tau_t + 5\tau_r\tau_t^2 + 5\tau_t^3) \\ & + 15c_r^2 c_t^4(\tau_r^3 + 5\tau_r^2\tau_t + 15\tau_r\tau_t^2 + 35\tau_t^3) + 2c_r c_t^5(5\tau_r^3 + 45\tau_r^2\tau_t + 315\tau_r\tau_t^2 - 3123\tau_t^3) \\ & + c_t^6(5\tau_r^3 + 105\tau_r^2\tau_t - 3123\tau_r\tau_t^2 + 4329\tau_t^3)\Big] - \ln\left(\frac{r_r}{r_t}\right)\left[1680 c_r c_t^5 \tau_t^3 + 840 c_t^6(\tau_r\tau_t^2 - 3\tau_t^3)\right]\end{aligned} \tag{B.18}$$

$$\begin{aligned}\gamma_c = 4\Big[& c_r^6(90\tau_r^3 + 40\tau_r^2\tau_t + 14\tau_r\tau_t^2 + 3\tau_t^3) + 2c_r^5 c_t(40\tau_r^3 + 42\tau_r^2\tau_t + 27\tau_r\tau_t^2 + 10\tau_t^3) \\ & + 5c_r^4 c_t^2(14\tau_r^3 + 27\tau_r^2\tau_t + 30\tau_r\tau_t^2 + 20\tau_t^3) + 20c_r^3 c_t^3(3\tau_r^3 + 10\tau_r^2\tau_t + 20\tau_r\tau_t^2 + 30\tau_t^3) \\ & + 5c_r^2 c_t^4(10\tau_r^3 + 60\tau_r^2\tau_t + 270\tau_r\tau_t^2 - 1089\tau_t^3) + 2c_r c_t^5(20\tau_r^3 + 270\tau_r^2\tau_t - 3267\tau_r\tau_t^2 + 996\tau_t^3) \\ & + 3c_t^6(10\tau_r^3 - 363\tau_r^2\tau_t + 332\tau_r\tau_t^2 + 840\tau_t^3)\Big] \\ & + 1680\ln\left(\frac{r_r}{r_t}\right)\left[5c_r^2 c_t^4\tau_t^3 + 2c_r c_t^5(3\tau_r\tau_t^2 - 4\tau_t^3) + c_t^6(\tau_r^2\tau_t - 4\tau_r\tau_t^2)\right]\end{aligned} \tag{B.19}$$

$$\begin{aligned}\gamma_d = -14\Big[& c_r^6(120\tau_r^3 + 56\tau_r^2\tau_t + 21\tau_r\tau_t^2 + 5\tau_t^3) + 2c_r^5 c_t(56\tau_r^3 + 63\tau_r^2\tau_t + 45\tau_r\tau_t^2 + 20\tau_t^3) \\ & + 15c_r^4 c_t^2(7\tau_r^3 + 15\tau_r^2\tau_t + 20\tau_r\tau_t^2 + 20\tau_t^3) + 20c_r^3 c_t^3(5\tau_r^3 + 20\tau_r^2\tau_t + 60\tau_r\tau_t^2 - 117\tau_t^3) \\ & + 5c_r^2 c_t^4(20\tau_r^3 + 180\tau_r^2\tau_t - 1053\tau_r\tau_t^2 - 21\tau_t^3) + 6c_r c_t^5(20\tau_r^3 - 351\tau_r^2\tau_t - 21\tau_r\tau_t^2 + 280\tau_t^3) \\ & + 3c_t^6(-39\tau_r^3 - 7\tau_r^2\tau_t + 280\tau_r\tau_t^2 + 280\tau_t^3)\Big] - 840\ln\left(\frac{r_r}{r_t}\right)\Big[20c_r^3 c_t^3\tau_t^3 + 5c_r^2 c_t^4(9\tau_r\tau_t^2 - 7\tau_t^3) \\ & + 6c_r c_t^5(3\tau_r^2\tau_t - 7\tau_r\tau_t^2) + c_t^6(\tau_r^3 - 7\tau_r^2\tau_t)\Big]\end{aligned} \tag{B.20}$$

$$\begin{aligned}\gamma_e = 28\Big[& c_r^6(168\tau_r^3 + 84\tau_r^2\tau_t + 35\tau_r\tau_t^2 + 10\tau_t^3) + 6c_r^5 c_t(28\tau_r^3 + 35\tau_r^2\tau_t + 30\tau_r\tau_t^2 + 20\tau_t^3) \\ & + 5c_r^4 c_t^2(35\tau_r^3 + 90\tau_r^2\tau_t + 180\tau_r\tau_t^2 - 174\tau_t^3) + 20c_r^3 c_t^3(10\tau_r^3 + 60\tau_r^2\tau_t - 174\tau_r\tau_t^2 - 33\tau_t^3) \\ & + 15c_r^2 c_t^4(20\tau_r^3 - 174\tau_r^2\tau_t - 99\tau_r\tau_t^2 + 70\tau_t^3) + 2c_r c_t^5(-174\tau_r^3 - 297\tau_r^2\tau_t + 630\tau_r\tau_t^2 + 280\tau_t^3) \\ & + c_t^6(-33\tau_r^3 + 210\tau_r^2\tau_t + 280\tau_r\tau_t^2 + 420\tau_t^3)\Big] + 1680\ln\left(\frac{r_r}{r_t}\right)\Big[10c_r^4 c_t^2\tau_t^3 + 20c_r^3 c_t^3(2\tau_r\tau_t^2 - \tau_t^3) \\ & + 15c_r^2 c_t^4(2\tau_r^2\tau_t - 3\tau_r\tau_t^2) + 2c_r c_t^5(2\tau_r^3 - 9\tau_r^2\tau_t) - c_t^6\tau_r^3\Big]\end{aligned} \tag{B.21}$$

$$\gamma_f = -70\Big[c_r^6(126\tau_r^3 + 70\tau_r^2\tau_t + 35\tau_r\tau_t^2 + 15\tau_t^3) + 10c_r^5c_t(14\tau_r^3 + 21\tau_r^2\tau_t + 27\tau_r\tau_t^2 - 12\tau_t^3) + 25c_r^4c_t^2(7\tau_r^3 + 27\tau_r^2\tau_t - 36\tau_r\tau_t^2 - 12\tau_t^3) + 300c_r^3c_t^3(\tau_r^3 - 4\tau_r^2\tau_t - 4\tau_r\tau_t^2 + \tau_t^3) - 25c_r^2c_t^4(12\tau_r^3 + 36\tau_r^2\tau_t - 27\tau_r\tau_t^2 - 7\tau_t^3) - 10c_rc_t^5(12\tau_r^3 - 27\tau_r^2\tau_t - 21\tau_r\tau_t^2 - 14\tau_t^3) + c_t^6(15\tau_r^3 + 35\tau_r^2\tau_t + 70\tau_r\tau_t^2 + 126\tau_t^3)\Big] + 4200\ln\left(\frac{r_r}{r_t}\right)\Big[-2c_r^5c_t\tau_t^3 - 5c_r^4c_t^2(3\tau_r\tau_t^2 - \tau_t^3) - 20c_r^3c_t^3(\tau_r^2\tau_t - \tau_r\tau_t^2) - 5c_r^2c_t^4(\tau_r^3 - 3\tau_r^2\tau_t) + 2c_rc_t^5\tau_r^3\Big] \quad \text{(B.22)}$$

$$\gamma_g = 28\Big[c_r^6(420\tau_r^3 + 280\tau_r^2\tau_t + 210\tau_r\tau_t^2 - 33\tau_t^3) + 2c_r^5c_t(280\tau_r^3 + 630\tau_r^2\tau_t - 297\tau_r\tau_t^2 - 174\tau_t^3) + 15c_r^4c_t^2(70\tau_r^3 - 99\tau_r^2\tau_t - 174\tau_r\tau_t^2 + 20\tau_t^3) + 20c_r^3c_t^3(-33\tau_r^3 - 174\tau_r^2\tau_t + 60\tau_r\tau_t^2 + 10\tau_t^3) + 5c_r^2c_t^4(-174\tau_r^3 + 180\tau_r^2\tau_t + 90\tau_r\tau_t^2 + 35\tau_t^3) + 6c_rc_t^5(20\tau_r^3 + 30\tau_r^2\tau_t + 35\tau_r\tau_t^2 + 28\tau_t^3) + c_t^6(10\tau_r^3 + 35\tau_r^2\tau_t + 84\tau_r\tau_t^2 + 168\tau_t^3)\Big] + 1680\ln\left(\frac{r_r}{r_t}\right)\Big[c_r^6\tau_t^3 + 2c_r^5c_t(9\tau_r\tau_t^2 - 2\tau_t^3) + 15c_r^4c_t^2(3\tau_r^2\tau_t - 2\tau_r\tau_t^2) + 20c_r^3c_t^3(\tau_r^3 - 2\tau_r^2\tau_t) - 10c_r^2c_t^4\tau_r^3\Big] \quad \text{(B.23)}$$

$$\gamma_h = 14\Big[3c_r^6(-280\tau_r^3 - 280\tau_r^2\tau_t + 7\tau_r\tau_t^2 + 39\tau_t^3) + 6c_r^5c_t(-280\tau_r^3 + 21\tau_r^2\tau_t + 351\tau_r\tau_t^2 - 20\tau_t^3) + 5c_r^4c_t^2(21\tau_r^3 + 1053\tau_r^2\tau_t - 180\tau_r\tau_t^2 - 20\tau_t^3) + 20c_r^3c_t^3(117\tau_r^3 - 60\tau_r^2\tau_t - 20\tau_r\tau_t^2 - 5\tau_t^3) + 15c_r^2c_t^4(-20\tau_r^3 - 20\tau_r^2\tau_t - 15\tau_r\tau_t^2 - 7\tau_t^3) + 2c_rc_t^5(-20\tau_r^3 - 45\tau_r^2\tau_t - 63\tau_r\tau_t^2 - 56\tau_t^3) + c_t^6(-5\tau_r^3 - 21\tau_r^2\tau_t - 56\tau_r\tau_t^2 - 120\tau_t^3)\Big] - 840\ln\left(\frac{r_r}{r_t}\right)\Big[c_r^6(7\tau_r\tau_t^2 - \tau_t^3) + 6c_r^5c_t(7\tau_r^2\tau_t - 3\tau_r\tau_t^2) + 5c_r^4c_t^2(7\tau_r^3 - 9\tau_r^2\tau_t) - 20c_r^3c_t^3\tau_r^3\Big] \quad \text{(B.24)}$$

$$\gamma_i = 4\Big[3c_r^6(840\tau_r^3 + 332\tau_r^2\tau_t - 363\tau_r\tau_t^2 + 10\tau_t^3) + 2c_r^5c_t(996\tau_r^3 - 3267\tau_r^2\tau_t + 270\tau_r\tau_t^2 + 20\tau_t^3) + 5c_r^4c_t^2(-1089\tau_r^3 + 270\tau_r^2\tau_t + 60\tau_r\tau_t^2 + 10\tau_t^3) + 20c_r^3c_t^3(30\tau_r^3 + 20\tau_r^2\tau_t + 10\tau_r\tau_t^2 + 3\tau_t^3) + 5c_r^2c_t^4(20\tau_r^3 + 30\tau_r^2\tau_t + 27\tau_r\tau_t^2 + 14\tau_t^3) + 2c_rc_t^5(10\tau_r^3 + 27\tau_r^2\tau_t + 42\tau_r\tau_t^2 + 40\tau_t^3) + c_t^6(3\tau_r^3 + 14\tau_r^2\tau_t + 40\tau_r\tau_t^2 + 90\tau_t^3)\Big] + 1680\ln\left(\frac{r_r}{r_t}\right)\Big[4c_r^6\tau_r^2\tau_t - c_r^6\tau_r\tau_t^2 + 8c_r^5c_t\tau_r^3 - 6c_r^5c_t\tau_r^2\tau_t - 5c_r^4c_t^2\tau_r^3\Big] \quad \text{(B.25)}$$

$$\gamma_j = -\Big[c_r^6(4329\tau_r^3 - 3123\tau_r^2\tau_t + 105\tau_r\tau_t^2 + 5\tau_t^3) + 2c_r^5c_t(-3123\tau_r^3 + 315\tau_r^2\tau_t + 45\tau_r\tau_t^2 + 5\tau_t^3) + 15c_r^4c_t^2(35\tau_r^3 + 15\tau_r^2\tau_t + 5\tau_r\tau_t^2 + \tau_t^3) + 20c_r^3c_t^3(5\tau_r^3 + 5\tau_r^2\tau_t + 3\tau_r\tau_t^2 + \tau_t^3) + 5c_r^2c_t^4(5\tau_r^3 + 9\tau_r^2\tau_t + 9\tau_r\tau_t^2 + 5\tau_t^3) + 6c_rc_t^5(\tau_r^3 + 3\tau_r^2\tau_t + 5\tau_r\tau_t^2 + 5\tau_t^3) + c_t^6(\tau_r^3 + 5\tau_r^2\tau_t + 15\tau_r\tau_t^2 + 35\tau_t^3)\Big] + 840\ln\left(\frac{r_r}{r_t}\right)\Big[-3c_r^6\tau_r^3 + c_r^6\tau_r^2\tau_t + 2c_r^5c_t\tau_r^3\Big] \quad \text{(B.26)}$$

$$\gamma_k = -280c_r^6\tau_r^3 \quad \text{(B.27)}$$

$$T_{0,2,0} = \int_0^{2\pi}\cos^2\varphi\int_{r_r}^{r_t}r^3\int_{-\frac{1}{2}h(r)}^{\frac{1}{2}h(r)}dxdrd\varphi = \frac{1}{120}N_b\upsilon_0\left(r_r^3\gamma_l + r_r^2r_t\gamma_m + r_rr_t^2\gamma_n + r_t^3\gamma_o\right) \quad \text{(B.28)}$$

$$T_{0,0,2} = \int_0^{2\pi} \sin^2\varphi \int_{r_r}^{r_t} r^3 \int_{-\frac{1}{2}h(r)}^{\frac{1}{2}h(r)} dx dr d\varphi$$
$$= \frac{1}{120} N_b \upsilon_0 \left(r_r^3 \gamma_l + r_r^2 r_t \gamma_m + r_r r_t^2 \gamma_n + r_t^3 \gamma_o \right) \tag{B.29}$$

where

$$\gamma_l = -\tau_r \left(10c_r^2 + 4c_r c_t + c_t^2 \right) - \tau_t \left(2c_r^2 + 2c_r c_t + c_t^2 \right) \tag{B.30}$$
$$\gamma_m = \tau_r \left(6c_r^2 - c_t^2 \right) - \tau_t \left(2c_r c_t + 3c_t^2 \right) \tag{B.31}$$
$$\gamma_n = \tau_r \left(3c_r^2 + 2c_r c_t \right) + \tau_t \left(c_r^2 - 6c_t^2 \right) \tag{B.32}$$
$$\gamma_o = \tau_r \left(c_r^2 + 2c_r c_t + 2c_t^2 \right) + \tau_t \left(c_r^2 + 4c_r c_t + 10c_t^2 \right) \tag{B.33}$$

In summary, these integrals can be written as

$$T_{0,0,0} = \frac{1}{12} N_b \kappa_a \upsilon_0 \left(r_t - r_r \right) \tag{B.34}$$
$$T_{1,0,0} = T_{0,1,0} = T_{0,0,1} = T_{1,1,0} = T_{1,0,1} = T_{0,1,1} = 0 \tag{B.35}$$
$$T_{2,0,0} = N_b^3 \upsilon_0^3 \frac{\gamma_a r_r^{10} + \gamma_b r_r^9 r_t + \gamma_c r_r^8 r_t^2 + \gamma_d r_r^7 r_t^3 + \gamma_e r_r^6 r_t^4 + \gamma_f r_r^5 r_t^5 + \gamma_g r_r^4 r_t^6 + \gamma_h r_r^3 r_t^7 + \gamma_i r_r^2 r_t^8 + \gamma_j r_r r_t^9 + \gamma_k r_t^{10}}{13440\pi^2 r_r r_t (r_r - r_t)^9} \tag{B.36}$$
$$T_{0,2,0} = T_{0,0,2} = \frac{1}{120} N_b \upsilon_0 \left(r_r^3 \gamma_l + r_r^2 r_t \gamma_m + r_r r_t^2 \gamma_n + r_t^3 \gamma_o \right) \tag{B.37}$$

C. Wing-Segment Thickness Distribution Integrals

As can be surmised from the integrations performed above, the effect of thickness distribution and corresponding υ factors is agnostic to the other geometric dimensions of the wing (and vice versa). We could thus determine the thickness distribution effects inside the integration by finding the ratio of the thickness distribution effects with and without the distribution considered. The thickness distribution υ terms for an airfoil with arbitrary thickness distribution can then be calculated as

$$\upsilon_0 \equiv \frac{\int_0^1 \mu(\hat{x}) d\hat{x}}{\int_0^1 d\hat{x}} \equiv \int_0^1 \mu(\hat{x}) d\hat{x} \tag{C.1}$$
$$\upsilon_1 \equiv \frac{\int_0^1 \left(\frac{1}{4} - \hat{x} \right) \mu(\hat{x}) d\hat{x}}{\int_0^1 \left(\frac{1}{4} - \hat{x} \right) d\hat{x}} \equiv -4 \int_0^1 \left(\frac{1}{4} - \hat{x} \right) \mu(\hat{x}) d\hat{x} \tag{C.2}$$
$$\upsilon_2 \equiv \frac{\int_0^1 \left(\frac{1}{4} - \hat{x} \right)^2 \mu(\hat{x}) d\hat{x}}{\int_0^1 \left(\frac{1}{4} - \hat{x} \right)^2 d\hat{x}} \equiv \frac{48}{7} \int_0^1 \left(\frac{1}{4} - \hat{x} \right)^2 \mu(\hat{x}) d\hat{x} \tag{C.3}$$
$$\upsilon_3 \equiv \frac{\int_0^1 \mu(\hat{x})^3 d\hat{x}}{\int_0^1 d\hat{x}} \equiv \int_0^1 \mu(\hat{x})^3 d\hat{x} \tag{C.4}$$

The υ_m, υ_n, and υ_o terms are not included here because the calculations for $S_{0,0,1} = S_{1,0,1} = S_{0,1,1} = 0$ as shown in Appendix A.

This approach can be applied to an airfoil with the NACA 4-digit thickness distribution

$$\mu(\hat{x}) = a_0 \sqrt{\hat{x}} + a_1 \hat{x} + a_2 \hat{x}^2 + a_3 \hat{x}^3 + a_4 \hat{x}^4$$

This results in the thickness distribution coefficients

$$\upsilon_0 = \frac{1}{60}\left(40a_0 + 30a_1 + 20a_2 + 15a_3 + 12a_4\right)$$
$$\upsilon_1 = \frac{1}{60}\left(56a_0 + 50a_1 + 40a_2 + 33a_3 + 28a_4\right)$$
$$\upsilon_2 = \frac{1}{980}\left(856a_0 + 770a_1 + 644a_2 + 553a_3 + 484a_4\right)$$
$$\begin{aligned}\upsilon_3 = {} & \frac{2}{5}a_0^3 + a_0^2a_1 + \frac{3}{4}a_0^2a_2 + \frac{3}{5}a_0^2a_3 + \frac{1}{2}a_0^2a_4 + \frac{6}{7}a_0a_1^2 + \frac{4}{3}a_0a_1a_2 + \frac{12}{11}a_0a_1a_3 + \frac{12}{13}a_0a_1a_4 \\ & + \frac{6}{11}a_0a_2^2 + \frac{12}{13}a_0a_2a_3 + \frac{4}{5}a_0a_2a_4 + \frac{2}{5}a_0a_3^2 + \frac{12}{17}a_0a_3a_4 + \frac{6}{19}a_0a_4^2 + \frac{1}{4}a_1^3 + \frac{3}{5}a_1^2a_2 \\ & + \frac{1}{2}a_1^2a_3 + \frac{3}{7}a_1^2a_4 + \frac{1}{2}a_1a_2^2 + \frac{6}{7}a_1a_2a_3 + \frac{3}{4}a_1a_2a_4 + \frac{3}{8}a_1a_3^2 + \frac{2}{3}a_1a_3a_4 + \frac{3}{10}a_1a_4^2 \\ & + \frac{1}{7}a_2^3 + \frac{3}{8}a_2^2a_3 + \frac{1}{3}a_2^2a_4 + \frac{1}{3}a_2a_3^2 + \frac{3}{5}a_2a_3a_4 + \frac{3}{11}a_2a_4^2 + \frac{1}{10}a_3^3 + \frac{3}{11}a_3^2a_4 + \frac{1}{4}a_3a_4^2 + \frac{1}{13}a_4^3\end{aligned}$$

This approach can similarly be applied to a diamond airfoil with thickness distribution

$$\mu(\hat{x}) = \begin{cases} \frac{\hat{x}}{\hat{x}_{mt}}, & 0 \le \hat{x} \le \hat{x}_{mt} \\ \frac{1-\hat{x}}{1-\hat{x}_{mt}}, & \hat{x}_{mt} \le \hat{x} \le 1 \end{cases}$$

where $\hat{x}_{mt}$ is the max thickness location in percent chord. This results in the thickness distribution coefficients

$$\upsilon_0 = \frac{1}{2}$$
$$\upsilon_1 = \frac{4\hat{x}_{mt} + 1}{6}$$
$$\upsilon_2 = \frac{8\hat{x}_{mt}^2 + 3}{14}$$
$$\upsilon_3 = \frac{1}{4}$$

D. Geometric and Mass Properties

A. Mass Properties – Validity Study : A Simple Foam Wing

Table D.1 Solid Works™ model mass characteristics of wings in simple wing study.

name	m [slugs]	x_{cg} [ft]	y_{cg} [ft]	z_{cg} [ft]]
rectangular	0.1644	-0.1704	4.0000	0.0000
taper	0.1781	-0.1966	2.7693	0.0000
thickness	0.1642	-0.1709	3.5550	0.0000
camber	0.1649	-0.1706	4.0000	-0.0272
clark y	0.1620	-0.1701	4.0000	-0.0306
diamond	0.1200	-0.2500	4.0000	0.0000
sweep	0.1644	-1.1677	4.0000	0.0000
all	0.1997	-0.8178	2.4716	-0.0323

The mass properties shown below in Tables D.2 and D.4 were calculated using the Traditional NACA 4-Digit Series thickness (or Clark Y for the Clark Y case) distribution coefficients presented in Table 1. The diamond airfoil case was calculated using the diamond airfoil υ values presented in Appendix C.

Table D.2 Calculated mass characteristics of wings in simple wing study.

name	m [slugs]	x_{cg} [ft]	y_{cg} [ft]	z_{cg} [ft]]
rectangular	0.1644	-0.1704	4.0000	0.0000
taper	0.1781	-0.1967	2.7692	0.0000
thickness	0.1644	-0.1704	3.5556	0.0000
camber	0.1644	-0.1704	4.0000	0.0000
clark y	0.1620	-0.1707	4.0000	0.0000
diamond	0.1200	-0.2500	4.0000	0.0000
sweep	0.1644	-1.1677	4.0000	0.0000
all	0.1964	-0.8156	2.4558	0.0000

Table D.3 Solid Works^{TM} model inertial characteristics of wings in simple wing study.

name, inertia [slugs-ft^2]	I_{xx_c}	I_{yy_c}	I_{zz_c}	I_{xy_c}	I_{xz_c}	I_{yz_c}
rectangular	0.8771	0.0092	0.8860	0.0000	0.0000	0.0000
taper	0.7389	0.0143	0.7527	0.0157	0.0000	0.0000
thickness	0.8439	0.0092	0.8528	0.0000	0.0000	0.0000
camber	0.8794	0.0093	0.8884	0.0000	0.0003	0.0000
Clark Y	0.8639	0.0090	0.8726	0.0000	0.0000	0.0000
diamond	0.6401	0.0051	0.6450	0.0000	0.0000	0.0000
sweep	0.8771	0.0637	0.9405	-0.2186	0.0000	0.0000
all	0.7297	0.0546	0.7835	-0.1660	0.0000	0.0025

Table D.4 Calculated inertial characteristics of wings in simple wing study.

name, inertia [slugs-ft^2]	I_{xx_c}	I_{yy_c}	I_{zz_c}	I_{xy_c}	I_{xz_c}	I_{yz_c}
rectangular	0.8770	0.0092	0.8860	0.0000	0.0000	0.0000
taper	0.7388	0.0143	0.7527	0.0157	0.0000	0.0000
thickness	0.8446	0.0092	0.8535	0.0000	0.0000	0.0000
camber	0.8770	0.0092	0.8860	0.0000	0.0000	0.0000
Clark Y	0.8639	0.0090	0.8727	0.0000	0.0000	0.0000
diamond	0.6401	0.0051	0.6450	0.0000	0.0000	0.0000
sweep	0.8770	0.0637	0.9405	-0.2186	0.0000	0.0000
all	0.7159	0.0536	0.7688	-0.1632	0.0000	0.0000

B. Geometric and Mass Properties – Assumption Study : Common Research Model

Note: the tip properties of each section (i.e. c_t, τ_t) are the same as those of the root of the following section ($c_{t_2} = c_{r_3}$).

Table D.5 Geometry of wing sections used in the CRM model.

wing	segment	b [ft]	c_r [ft]	τ_r [%]	$x_{c_r/4}$ [ft]	$y_{c_r/4}$ [ft]	$z_{c_r/4}$ [ft]	Γ [deg]	Λ [deg]
main wing	1	2.93750	44.67224	7.62378	0.00000	0.00000	0.00000	1.83545	29.85541
	2	1.46897	39.03412	6.78517	-5.53181	9.63251	-0.30868	3.05240	30.56131
	3	1.46900	36.21522	6.35253	-8.37764	14.44514	-0.56531	2.23495	31.41867
	4	1.46900	33.39567	5.97035	-11.32166	19.26101	-0.75326	2.16505	31.62033
	5	1.46900	30.57644	5.66899	-14.28902	24.07712	-0.93534	2.34430	31.64957
	6	1.46900	27.75722	5.44749	-17.25978	28.89264	-1.13248	2.40660	31.39684
	7	0.58760	24.93766	5.29470	-20.20129	33.70795	-1.33485	2.45945	32.01123
	8	0.88140	23.81004	5.25501	-21.40645	35.63399	-1.41758	2.75120	34.32199
	9	1.46899	23.10236	5.18539	-23.38067	38.52238	-1.55638	3.33140	35.25116
	10	1.46899	21.92290	5.09244	-26.78693	43.33377	-1.83645	3.92060	34.93690
	11	1.46899	20.74344	4.99603	-30.15370	48.14202	-2.16598	4.50280	35.02215
	12	1.46899	19.56398	4.92971	-33.53114	52.94668	-2.54435	5.08865	34.99820
	13	1.46899	18.38419	4.87321	-36.90559	57.74722	-2.97183	5.70810	35.00452
	14	1.46899	17.20472	4.82710	-40.28083	62.54284	-3.45118	6.45865	35.00456
	15	1.46899	16.02526	4.77676	-43.65606	67.33177	-3.99331	7.23240	35.00130
	16	1.46899	14.84580	4.74344	-47.03089	72.11294	-4.60006	8.01395	34.99822
	17	1.46899	13.66601	4.71523	-50.40532	76.88539	-5.27197	8.75975	35.00101
	18	1.46899	12.48655	4.69384	-53.78012	81.64870	-6.00594	9.42520	35.00339
	19	1.46900	11.30709	4.68028	-57.15521	86.40317	-6.79519	9.93525	35.00275
	20	1.46900	10.12762	4.67588	-60.53024	91.15043	-7.62673	9.98105	34.99848
	tip	-	8.94816	4.58818	-	-	-	-	-
horizontal stabilizer	1	2.13360	18.84546	4.92665	-98.91770	0.00000	-7.53755	7.51132	37.00000
	2	1.06680	18.42119	4.91130	-104.19258	6.93993	-8.45260	7.51132	37.00000
	3	1.06680	17.04348	4.85629	-106.83002	10.40990	-8.91013	7.51132	37.00000
	4	1.06680	15.66591	4.79190	-109.46746	13.87987	-9.36765	7.51132	37.00000
	5	1.06680	14.28849	4.71577	-112.10490	17.34983	-9.82518	7.51132	37.00000
	6	1.06680	12.91130	4.62444	-114.74234	20.81980	-10.28271	7.51132	37.00000
	7	1.06680	11.53439	4.51323	-117.37978	24.28977	-10.74024	7.51132	37.00000
	8	1.06680	10.15790	4.37582	-120.01721	27.75973	-11.19776	7.51132	37.00000
	9	1.06680	8.78202	4.20530	-122.65465	31.22970	-11.65529	7.51132	37.00000
	tip	-	7.40336	3.99248	-	-	-	-	-

The present method mass properties shown below in Tables D.6 and D.7 were calculated using the Traditional NACA 4-Digit Series thickness distribution coefficients presented in Table 1.

Table D.6 Mass characteristics of analyses in CRM model study.

Analysis	m [slugs]	x_{cg} [ft]	y_{cg} [ft]	z_{cg} [ft]]
OML	15091.2293	-28.2241	0.0000	-1.2547
uncambered	15091.2293	-28.0030	0.0000	-1.4925
no twist	15091.2293	-28.0255	0.0000	-1.8191
straight quarter-chord	15091.2293	-28.0276	0.0000	-1.8356
present method	15091.2367	-28.0271	0.0000	-1.8355

Table D.7 Inertial characteristics of analyses in CRM model study.

Analysis, inertia [slugs-ft^2]	I_{xx_c}	I_{yy_c}	I_{zz_c}	I_{xy_c}	I_{xz_c}	I_{yz_c}
OML	14,566,029	13,351,211	27,577,684	0	1,262,327	0
uncambered	14,453,198	13,248,794	27,428,889	2	1,160,878	0
no twist	14,448,038	13,240,193	27,461,809	0	1,140,055	0
straight quarter-chord	14,448,965	13,237,963	27,462,065	-3	1,135,757	0
present method	14,448,167	13,236,697	27,460,029	0	1,135,642	0

C. Geometric and Mass Properties – Constant Density Assumption Study : Horizon

Note: the tip properties of each section (i.e. c_t, τ_t) are the same as those of the root of the following section ($c_{t_2} = c_{r_3}$). Also note

Table D.8 Geometry of wing sections used in the Horizon model.

segment	b [ft]	c_r [ft]	τ_r [%]	$x_{c_r/4}$ [ft]	$y_{c_r/4}$ [ft]	$z_{c_r/4}$ [ft]	Γ [deg]	Λ [deg]
1	0.37500	2.75000	12.00000	0.00000	0.00000	0.00000	0.37805	1.53147
2	0.42500	2.75000	12.00000	-0.01003	0.37499	-0.00247	1.18455	4.79895
3	1.28530	1.14583	12.00000	-0.04571	0.79989	-0.01126	2.90887	11.81543
4	1.15951	1.07502	12.00000	-0.31458	2.08354	-0.07649	5.37374	21.81725
5	0.92021	1.01113	12.00000	-0.77876	3.23795	-0.18508	7.47049	30.30459
6	0.59083	0.96043	12.00000	-1.31658	4.15036	-0.30472	8.99387	36.45067
7	0.20359	0.92788	12.00000	-1.75299	4.73392	-0.39708	9.79476	39.67215
8	0.22788	0.91667	12.00000	-1.92184	4.93454	-0.43172	50.00000	45.83747
9	0.57750	0.74717	12.00000	-2.15648	5.08102	-0.60628	90.00000	53.54149
tip	-	0.34350	12.00000	-	-	-	-	-

The present method mass properties shown below in Tables D.9 and D.10 were calculated using the Traditional NACA 4-Digit Series thickness distribution coefficients presented in Table 1.

Table D.9 Mass characteristics of analyses in Horizon model study.

Analysis	m [slugs]	x_{cg} [ft]	y_{cg} [ft]	z_{cg} [ft]]
actual	0.3529	-0.7853	-0.0001	-0.1380
OML	0.3529	-0.6972	0.0000	-0.1265
uncambered	0.3529	-0.6984	0.0000	-0.0997
straight quarter-chord	0.3529	-0.7106	0.0000	-0.1019
present method	0.3529	-0.7106	0.0000	-0.1019

Table D.10 Inertial characteristics of analyses in Horizon model study.

Analysis, inertia [slugs-ft^2]	I_{xx_c}	I_{yy_c}	I_{zz_c}	I_{xy_c}	I_{xz_c}	I_{yz_c}
actual	2.2840	0.1715	2.4374	0.0000	0.0256	0.0000
OML	1.8386	0.1779	1.9977	0.0000	0.0274	0.0000
uncambered	1.8458	0.1791	2.0043	0.0000	0.0287	0.0000
straight quarter-chord	1.8409	0.1800	2.0000	0.0000	0.0291	0.0000
present method	1.8409	0.1800	2.0000	0.0000	0.0291	0.0000

Acknowledgements

This work was funded by the U.S. Office of Naval Research Sea-Based Aviation program (grant no. N00014-18-1-2502) with Brian Holm-Hansen as the Program Officer.

References

[1] Lanham, C., "Inertia Calculation Procedure for Preliminary Design," Tech. rep., AERONAUTICAL SYSTEMS DIV WRIGHT-PATTERSON AFB OH, 1979.

[2] Wolowicz, C. H., and Yancey, R. B., "Experimental determination of airplane mass and inertial characteristics," Tech. rep., NASA, 1974.

[3] Saltari, F., Riso, C., Matteis, G. D., and Mastroddi, F., "Finite-element-based modeling for flight dynamics and aeroelasticity of flexible aircraft," *Journal of Aircraft*, Vol. 54, No. 6, 2017, pp. 2350–2366.

[4] Cesnik, C., and Su, W., "Nonlinear aeroelastic modeling and analysis of fully flexible aircraft," *46th AIAA/ASME/ASCE/AHS/ASC Structures, Structural Dynamics and Materials Conference*, 2005, p. 2169.

[5] Jardin, M. R., and Mueller, E. R., "Optimized measurements of unmanned-air-vehicle mass moment of inertia with a bifilar pendulum," *Journal of Aircraft*, Vol. 46, No. 3, 2009, pp. 763–775.

[6] Habeck, J., and Seiler, P., "Moment of inertia estimation using a bifilar pendulum," *University of Minnesota*, 2016.

[7] Lorenzetti, J. S., Bañuelos, L., Clarke, R., Murillo, O. J., and Bowers, A., "Determining products of inertia for small scale UAVs," *55th AIAA Aerospace Sciences Meeting*, 2017, p. 0547.

[8] de Silva Bussamra, F. L., Vilchez, C. M. M., and Santos, J. C., "Experimental Determination of Unmanned Aircraft Inertial Properties," *3rd CTA-DLR Workshop on Data Analysis and Flight Control 2009 Brazilian Symposium on Aerospace Eng. & Applications*, 2009, pp. –.

[9] Soule, H. A., and Miller, M. P., "The experimental determination of the moments of inertia of airplanes," Tech. rep., Citeseer, 1934.

[10] du Bois, J. L., Lieven, N. A., and Adhikari, S., "Error analysis in trifilar inertia measurements," *Experimental Mechanics*, Vol. 49, No. 4, 2009, pp. 533–540.

[11] Gracey, W., "The experimental determination of the moments of inertia of airplanes by a simplified compound-pendulum method," Tech. rep., National Aeronautics and Space Administration Washingtion DC, 1948.

[12] Green, M., "Measurement of the moments of inertia of full scale airplanes," Tech. rep., National Aeronautics and Space Administration, 1927.

[13] De Jong, R., and Mulder, J., "Accurate estimation of aircraft inertia characteristics from a single suspension experiment," *Journal of Aircraft*, Vol. 24, No. 6, 1987, pp. 362–370.

[14] Lehmkühler, K., Wong, K., and Verstraete, D., "Methods for accurate measurements of small fixed wing UAV inertial properties," *The Aeronautical Journal*, Vol. 120, No. 1233, 2016, pp. 1785–1811.

[15] Previati, G., Gobbi, M., and Mastinu, G., "Method for the measurement of the inertia properties of bodies with aerofoils," *Journal of aircraft*, Vol. 49, No. 2, 2012, pp. 444–452.

[16] Perry, D., "Measurements of the Moments of Inertia of the Avro 707B Aircraft," *Ministry of Aviation*, 1963.

[17] Dantsker, O. D., Vahora, M., Imtiaz, S., and Caccamo, M., "High fidelity moment of inertia testing of unmanned aircraft," *2018 Applied Aerodynamics Conference*, 2018, p. 4219.

[18] Morelli, E. A., "Determining aircraft moments of inertia from flight test data," *Journal of Guidance, Control, and Dynamics*, Vol. 45, No. 1, 2022, pp. 4–14.

[19] Pegram, J. P., and Anemaat, W. A., "Preliminary estimation of airplane moments of inertia using CAD solid modeling," Tech. rep., SAE Technical Paper, 2000.

[20] Parikh, K., Dogan, A., Subbarao, K., Reyes, A., and Huff, B., "CAE tools for modeling inertia and aerodynamic properties of an RC airplane," *AIAA atmospheric flight mechanics conference*, 2009, p. 6043.

[21] Jordan, T., Langford, W., and Hill, J., "Airborne subscale transport aircraft research testbed-aircraft model development," *AIAA Guidance, Navigation, and Control Conference and Exhibit*, 2005, p. 6432.

[22] Bai, C., Mingqiang, L., Zhong, S., Zhe, W., Yiming, M., and Lei, F., "Wing weight estimation considering constraints of structural strength and stiffness in aircraft conceptual design," *International Journal of Aeronautical and Space Sciences*, Vol. 15, No. 4, 2014, pp. 383–395.

[23] Valencia, E., Alulema, V., Hidalgo, V., and Rodriguez, D., "A CAD-free methodology for volume and mass properties computation of 3-D lifting surfaces and wing-box structures," *Aerospace Science and Technology*, Vol. 108, 2021, p. 106378.

[24] do Vale, J. L., Sohst, M., Crawford, C., Suleman, A., Potter, G., and Banerjee, S., "On the multi-fidelity approach in surrogate-based multidisciplinary design optimisation of high-aspect-ratio wing aircraft," *The Aeronautical Journal*, 2022, pp. 1–22.

[25] Mutluay, T., "The Development of an Inertia Estimation Method to Support Handling Quality Assessment," -, 2015.

[26] Shigley, J. E., *Shigley's mechanical engineering design*, Tata McGraw-Hill Education, 2011.

[27] Greenwood, D. T., "Inertial Properties of Homogeneous Bodies," *Principles Of Dynamics*, Prentice Hall, New Jersey, 1988, pp. 533–536.

[28] Abbott, I. H., and Doenhoff, A. E. V., "Families of Wing Sections," *Theory of Wing Sections*, McGraw–Hill, New York, 1949, (republished by Dover, New York, 1959), Chap. 6, pp. 111–123.

[29] Hunsaker, D. F., Reid, J. T., and Joo, J. J., "Geometric Definition and Ideal Aerodynamic Performance of Parabolic Trailing-Edge Flaps," *International Journal of Astronautics and Aeronautical Engineering*, Vol. 4, No. 1, 2019, pp. 1–17.

[30] Phillips, W. F., "Aircraft Flight Simulation : Relations between the Quaternion and Other Attitude Descriptors," *Mechanics of Flight*, John Wiley and Sons, Inc., 2010, Chap. 11, 2nd ed., pp. 1004–1012.

[31] Phillips, W. F., "Aircraft Equations of Motion : Inertial and Gyroscopic Coupling," *Mechanics of Flight*, John Wiley and Sons, Inc., 2010, Chap. 7, 2nd ed., pp. 805–806.

[32] Taylor, J. D., and Hunsaker, D. F., "Characterization of the Common Research Model Wing for Low-Fidelity Aerostructural Analysis," *AIAA Scitech 2021 Forum*, 2021, p. 1591.